Semi-Classical Molecular Dynamics Simulations of Polariton Transport in Organic Molecules Strongly Coupled to Bloch Surface Waves

M.Sc. thesis

University of Jyväskylä

Department of Chemistry

Yunyi Luo

December 31, 2024

JYVÄSKYLÄN YLIOPISTO

Abstract

Author: Yunyi Luo

Supervisors: Professor Gerrit Groenhof ; Ilia Sokolovskii

Title: Semi-Classical Molecular Dynamics Simulations of Polariton Transport in Organic Molecules Strongly Coupled to Bloch Surface Waves

Strong coupling has emerged as a mechanism to extend the diffusion length of excitons in organic semiconductors beyond their typical limits. This phenomenon manifests itself in the formation of hybrid light-matter states, known as polaritons, which arise when the interaction strength between light (e.g., cavity modes) and matter (e.g., molecular excitons) exceeds the decay rates in the system, such as cavity losses and molecular deactivation. Because of their partially photonic nature, polaritons exhibit fast and long-range propagation, resulting in enhanced transport of excitation.

In this work, hybrid quantum mechanics/molecular mechanics simulations of polariton transport in a structure supporting Bloch Surface Waves were conducted to investigate the experimentally observed shift in the transport regime as the photonic contribution to polariton states changes. By comparing the results of molecular simulations with the results of simulations of static two-level systems, we analyze the origin of this shift and reveal the crucial role of molecular vibrations behind the shift. With the results, we demonstrate the critical role of selecting an appropriate model when simulating dynamics of polaritons. We expect that these insights provided in this thesis will be valuable for improving energy transfer in organic materials.

Keywords: strong coupling, polaritons, molecular dynamics

Preface

I am deeply grateful to the University of Jyväskylä and its supportive research environment for providing the foundation for this project. I especially want to thank my supervisors, Professor Gerrit Groenhof and Ilia Sokolovskii, for their expert guidance and invaluable feedback. The research group, including Dr. Dmitry Morozov, Dr. Arun Kanakati, Dr. Emmi Pohjolainen, and Santiago Gomez, also played a vital role in my progress through their helpful discussions and encouragement.

This Master's project began in the summer of 2023. My journey has not been without its challenges, including personal health setbacks. Through it all, the support and companionship of friends, both near and far, has been invaluable. I am particularly grateful to my friends in Finland, Zhiyang Feng, Xinyue Wang, and Yue Ding, for their constant support and companionship. I also want to thank my online friends: Effy Chen, Xiaoyu Li, Kailun Hong, Yujing Zhang, Bi Wang, Jiali He, Jine Wu, Hongrui Zeng, and Jiaheng Liu, for their constant presence and encouragement.

Most importantly, I want to thank my family for their unwavering love and support during my time in Finland. My deepest gratitude goes to my mother, whose courage and strength in her own health journey have been a true inspiration.

Jyväskylä, 25.12.2024

Yunyi Luo

Abbreviations

BSW	Bloch surface wave
DBR	distributed Bragg reflector
DFT	density functional theory
FP	Fabry-Pérot (microcavity)
LP	lower polariton
MD	molecular dynamics
MeB	Methylene Blue
MSD	mean squared displacement
PV	photovoltaics
QM/MM	quantum mechanics/molecular mechanics
TDDFT	time-dependent density functional theory
UP	upper polariton

AI Usage Disclosure

AI has been utilized in this thesis in the following manner:

1. **Introduction:** ChatGPT and DeepL were used for correcting grammar, translating and proofreading my text.

2. **Theoretical Background:** ChatGPT was used to summarize articles and was asked to provide feedback on my own text. DeepL was used for translation and proofreading my text.

3. **Conculsion:** DeepL was used for translation and proofreading my text and Writefull was used for correcting grammar.

Contents

1   Introduction

The growing imperative for environmental conservation and sustainable growth has increasingly spotlighted the use of energy as a critical global issue. From resource depletion to pollution and climate change, the drawbacks of conventional energy sources such as oil, natural gas, coal are increasingly apparent. To address these issues, a paradigm shift towards renewable and sustainable energy solutions is imperative.

As mentioned in the seventh goal of the United Nations on sustainable development, clean and affordable energy systems are key to ensuring development in all areas.[1] The potential of solar energy and its clean and limitless capabilities were explored 50 years ago, yet its use today accounts for only about one percent of the global energy supply.[2] While solar energy holds immense promise, its widespread integration into the global energy system remains a work in progress, underscoring the need for continuous innovation and technological breakthroughs. The rich potential of solar energy utilisation has led to tremendous value in research on solar energy, such as solar photovoltaics (PV) and solar thermal technologies.

Solar PV, with its direct conversion of sunlight to electricity without carbon emissions, has become a key area of focus. However, fully unlocking the potential of solar energy requires tackling several key challenges: boosting energy conversion efficiency, lowering production and installation costs, and ensuring the long-term reliability and resilience of solar panels under various environmental stresses. Thus, the exploration of new materials has become a promising frontier. The central aim is to improve cell efficiency, enhance durability and reduce costs. Within the spectrum of materials, organic and inorganic substances present contrasting advantages and limitations, each offering unique potential for energy applications.

Inorganic materials are the backbone of the PV market, with 90% of the materials being silicon-based.[3] Silicon-based materials are widely used in the PV market due to their technological maturity and mass production as well as their ease of installation.[4] However, silicon-based materials have a number of drawbacks, including the high temperatures required for processing, high energy consumption, and limited module efficiency.[5] In addition, the highest recorded efficiency of crystalline silicon technology (27.6 %)[6] is approaching its theoretical efficiency limit (29.4%)[7] . Therefore, further development of the PV market might require searching for other materials to complement or even replace silicon in solar cells.

Organic PV cells, which belong to the third generation of emerging solar cells after crystalline silicon and thin-film solar cells, are currently attracting the attention of the research community.[8] Organic materials exhibit flexibility and lower

production costs, making them appealing candidates for energy-related applications like smart power generation in clothing, portable cell phone chargers, and power-generating windows. Devices such as organic light-emitting diodes (OLEDs) are already making significant commercial impacts due to their ability to deliver more vibrant colors compared to conventional liquid crystalline screens.[9,10]

Despite these benefits, the actual share of organic materials in the PV market is low. There are a number of reasons for this, the most obvious being the low energy conversion efficiency of organic semiconductors. Commonly used silicon solar cells have achieved an efficiency of 24%,[11] while organic solar cells are struggling to reach 10% efficient. This performance deficit can be attributed to fundamental material characteristics, such as restricted charge transport, limited light absorption across the solar spectrum, and rapid recombination of excitons, all of which conspire to reduce the overall efficiency of energy conversion.[12,13,14] With this in mind, researchers are actively developing new materials and processing techniques to enhance the performance of organic photovoltaic devices. Achieving higher efficiencies is paramount for the widespread adoption of this technology, and thus, substantial efforts are dedicated to exploring methods that improve the efficiency of organic solar cells.

One promising avenue that has garnered significant interest is the concept of strong coupling,[15] which has been experimentally shown to improve the diffusion coefficient of molecular excitons by a few orders of magnitude.[9,16] Strong coupling involves the interaction between light and matter within microcavities, leading to the formation of hybrid states known as polaritons between the cavity electromagnetic field and the molecular excitons.[17,18,19] Polaritons exhibit a unique combination of light and matter properties, with a small effective mass and the ability to interact coherently, while also exhibiting high group velocity and a delocalized character.[20] These hybrid properties open up potential applications for exciton polaritons in PV devices. For instance, angle-resolved photodetection in microcavities has demonstrated the potential for efficient energy transport and ultrafast modulation of polariton states, paving the way for enhanced PV system performance.[21]

In this work, we focus specifically on the transport mechanisms of exciton-polaritons within the context of strong coupling phenomena. By employing the advanced quantum mechanics/molecular mechanics molecular dynamics simulations, our goal is to investigate the exciton-polariton transport in structures supporting Bloch Surface Waves and to provide valuable insights that could inform the development of advanced energy transport technologies.

2 Theoretical Background

In this chapter, the fundamentals of strong coupling will be firstly illustrated, including the mechanism and condition of achieving strong coupling, the properties of polaritons and their transport. Then different types of cavities as well as the simulation methods will be described.

2.1 The Fundamentals of Strong Coupling

In free space, the energy exchange between electromagnetic field and molecules is relatively weak due to short interaction times and relatively low interaction strength between the field and the molecules. To circumvent these constraints, researchers have turned to optical cavities that serve to confine the electromagnetic field and enhance the interaction with molecules. By confining light within the cavity, an environment can be created in which photons are reflected multiple times, thereby increasing the likelihood of interaction with the molecules within the cavity. This repeated interaction enhances the electric field experienced by the molecule, which in turn enhances the coupling to light. This process makes it possible to enter a strong coupling regime, where the molecules and the electromagnetic field are continuously exchanging energy resulting in the creation of hybrid light-matter states called polaritons.

The interaction between a single molecule and a single cavity light mode can be quantified using the *coupling strength*, denoted as g. Within the dipole approximation, the coupling strength is defined as:

$$g = -\hat{\boldsymbol{\mu}} \cdot \mathbf{E}_{\text{vac}}, \tag{1}$$

where $\hat{\boldsymbol{\mu}}$ is the transition dipole moment operator of the molecule, and $\mathbf{E}_{\text{vac}}$ is the vacuum electric field in the cavity. This relationship shows that the strength of the interaction depends directly on the molecule's dipole moment and the intensity of the local electric field inside the cavity.

When electromagnetic field is confined within an optical cavity, the molecule-light system enters a strong coupling regime, as the cavity facilitates the confinement of light, enabling prolonged interaction with molecules and thereby enhancing the strength of this interaction. This phenomenon entails the hybridization of molecular resonances (e.g., excitons or vibrational transitions) with electromagnetic field modes, leading to the formation of new hybrid states. The result of this hybridization is the disappearance of the original molecular and electromagnetic resonances, which were independent of each other. They are replaced by two new hybrid states,

called upper (UP) and lower (LP) polaritons, which carry properties of both cavity light modes and molecular excitations.[18]

2.1.1 Concept of Strong Coupling

Strong coupling occurs when the interaction rate between molecular excitation and the electromagnetic mode, defined by the coupling strength g, exceeds both the decay rate of the cavity mode κ and the decay rate of the molecular excitation γ. In this regime, the system continuously exchanges energy between light and matter before dissipation occurs, giving rise to Rabi oscillations, which manifest as a periodic exchange of energy.

Commonly, the condition for strong coupling is expressed as:

$$g > \kappa, \gamma. \tag{2}$$

The quality factor Q of the cavity determines how long the cavity can trap light, and it is inversely proportional to κ by the equation:

$$\kappa = \frac{\omega}{Q}, \tag{3}$$

where ω is the resonant frequency of the cavity mode.

When this condition is met, the single molecular resonance splits into two new polaritonic states, which correspond to the upper and lower polaritons.[22] The energy difference between these states is known as the Rabi splitting, $\hbar\Omega_R$.

The energy levels of the hybridized system are shifted by an amount proportional to the coupling strength g. For a single molecule, the Rabi splitting between the polariton states is given by:

$$\hbar\Omega_R = 2g. \tag{4}$$

This splitting can be observed experimentally through absorption or reflection spectra, where the presence of two peaks, rather than one, confirms that the system has entered the strong coupling regime.[23]

2.1.2 Role of the Mode Volume and Vacuum Electric Field

The strength of the light-matter interaction within a cavity is influenced by the mode volume V_{mode} of the cavity, which represents the spatial confinement of the electromagnetic field. A smaller mode volume leads to a stronger local electric field, which, in turn, increases the coupling strength. The vacuum electric field $\mathbf{E}_{\mathrm{vac}}$ inside the cavity is inversely proportional to the square root of the mode volume, as shown in the following relationship:

$$\mathbf{E}_{\mathrm{vac}} \propto \sqrt{\frac{\hbar\omega_{\mathrm{vac}}}{2\epsilon_0\epsilon_{\mathrm{b}}V_{\mathrm{mode}}}}, \tag{5}$$

where $\hbar$ is the reduced Planck constant, ω_{vac} is the angular frequency of the cavity mode, ϵ_0 is the permittivity of free space, ϵ_b is the dielectric constant of the

cavity medium. Thus, by reducing the mode volume, the vacuum electric field $\mathbf{E}_{\text{vac}}$ increases, enhancing the interaction with the molecules. This is why nanophotonic structures and plasmonic cavities, with their smaller sizes, can achieve much stronger coupling compared to larger, traditional optical cavities.

2.1.3 Dark States in Strong Coupling

When the number of molecule is more than one, in addition to the bright polariton states, strong coupling also leads to the formation of dark states. These are collective molecular states that lack contribution from the cavity field, and therefore they cannot be excited by light. Dark states arise due to destructive interference among the molecules, where the dipole moments of different molecules cancel out.[23]

Dark states play a crucial role in the system's overall dynamics, particularly in the context of molecular ensembles with many molecules. Dark states can serve as energy reservoirs[24] and influence relaxation processes within the system.

2.2 Different Types of Cavities in Strong Coupling

To achieve strong coupling, various types of cavities can be used, each offering distinct advantages depending on the experimental setup and the desired interaction strength. Next we introduce two types of cavities: Fabry-Pérot (FP) cavities, which are the most commonly used in experiments due to their versatility and widespread application, and structures supporting Bloch Surface Waves, as our study specifically investigates polariton transport in this type of cavity.

2.2.1 Fabry-Pérot (FP) Cavity

Fabry-Pérot(FP, Figure 1) cavities are optical resonators that consist of two parallel reflective surfaces that trap light between them. This design allows for confinement of the electromagnetic field within the cavity volume. In the context of strong coupling, FP cavities play a crucial role in significantly enhancing the interaction between light and molecules because they support a large number of molecules that can collectively reach the strong coupling regime.[25,26]

By varying the distance between mirrors, FP cavities can be fine-tuned to optimize the resonance conditions for specific molecular transitions, making them a versatile tool for exploring and controlling polaritonic dynamics. This tunability makes FP cavities highly popular for applications in polaritonic chemistry, quantum optics, and light-driven molecular processes.
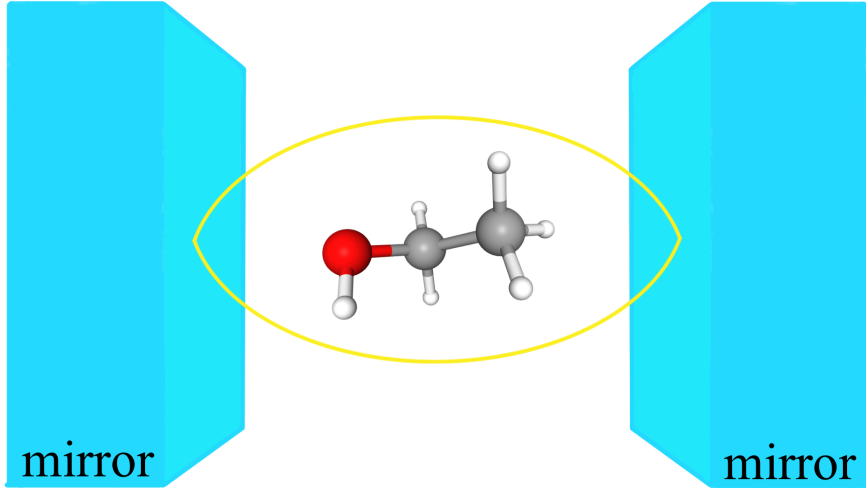
Figure 1. Schematic illustration of molecules located in a Fabry-Pérot (FP) cavity composed of two reflective mirrors. The yellow line is an intensity of the vacuum field associated with exciting the cavity with a single photon.

2.2.2 Structures supporting Bloch Surface Waves

Bloch Surface Waves (BSW, Figure 2) are electromagnetic surface waves that propagate along the interface between a truncated photonic crystal, such as a distributed Bragg reflector (DBR), and a dielectric medium. Unlike Surface Plasmon Polaritons, which are confined to metal-dielectric interfaces and suffer from high losses, BSW are supported by all-dielectric structures. This dielectric nature allows BSW to provide lower losses, hence higher quality factors,[27] and good light confinement, making them an excellent platform for enhancing strong coupling.[28]

The DBR structure represents a one-dimensional photonic crystal characterized by a periodic variation in dielectric permittivity, expressed as $\varepsilon(x) = \varepsilon(x+A)$, where A is the periodicity. This structure of periodically varying dielectric constant causes electromagnetic waves to be repeatedly reflected in it, leading to the formation of frequency ranges at which light can propagate through the crystal (pass bands) and ranges at which light is unable to propagate through the crystal (stop bands). At the same time, a localized state can form in the structure when a surface defect is introduced, such as a layer with a slightly different dielectric constant or thickness (as illustrated in Figure 2), which facilitates the emergence of the BSW, shown as the black line in Figure 2. In the context of strong coupling, BSW structures significantly enhance the local electromagnetic field at the interface, increasing the interaction between the optical mode and excitons of molecules. A key study by Liscidini *et al.* demonstrated that BSW can achieve stronger exciton-photon coupling than traditional microcavities, leading to larger Rabi splittings and more efficient polariton formation.[29] The ability to achieve such strong coupling at room temper-
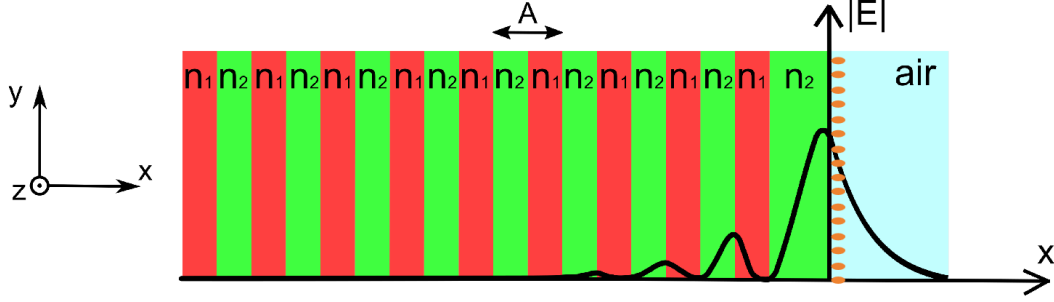
Figure 2. Schematic representation of a DBR structure supporting a BSW. The DBR consists of alternating layers with different refractive indices of n_1 and n_2 and a period of A along the x-axis. The side in contact with the air is a special layer with a refractive index of n_2 and a thickness different from that of the other layers. Between the DBR and the air is a row of orange ellipses, which represent the molecules. The electric field strength distribution of the BSW is shown as a black line.

ature was further confirmed by Lerario *et al.*, who observed the formation of BSW polaritons using J-aggregates of organic molecules at room temperature.[30]

BSW structures also offer exceptional tunability. By adjusting the thickness and refractive indices of the dielectric layers, the resonance frequency of the BSW can be finely tuned to match specific molecular transitions. This tunability allows BSW structures to be tailored for different applications, including sensing and spectroscopy, where the enhancement of light-matter interactions is critical. The low-loss, high-field enhancement properties of BSW cavities make them an ideal platform for sustaining strong coupling over longer periods of time.[30]

2.3   Polariton Transport

The distinctive transport characteristics of polaritons are attributable to their composite nature, comprising both matter and light. This enables polaritons to exhibit behaviours that diverge from those of conventional excitons. The formation of polaritons can facilitate enhanced transport, enabling both long-range diffusion and even ballistic motion in certain regimes.[9,31,32,33,34]

In traditional organic materials, the transport of excitons is dominated by a random hopping process between molecular sites, resulting in a slow, diffusive motion.[9] This process is constrained by the short-range nature of molecular interactions and is further limited by disorder in the material, which disrupts coherent energy transfer. Polaritons, in contrast, incorporate a photonic component that delocalises their wave functions over considerably greater distances than those available to bare excitons, thereby significantly enhancing transport. This hybridization enables long-range coherence, allowing polaritons to move across macroscopic distances more efficiently than conventional excitons, as evidenced by experiments where the diffusion coeffi-

cient of molecular excitons was enhanced by up to six orders of magnitude upon the formation of polariton.[20]

The mean squared displacement (MSD) was used to characterize excitation energy transport. MSD quantifies how far the excitation travels over time, t, and it is derived from the expectation value of the position operator $\hat{z}(t)$, which defines the average position of the wave function at a given time. The expectation value is expressed as:

$$
\begin{aligned}
\langle \hat{z}(t) \rangle &= \frac{\langle \Psi(t) | \hat{z}(t) | \Psi(t) \rangle}{\langle \Psi(t) | \Psi(t) \rangle} \\
\\
&= \frac{\sum_i^N z_i(t) |\Psi(t, z_i)|^2}{\sum_i^N |\Psi(t, z_i)|^2},
\end{aligned}
\tag{6}
$$

where $\Psi(t, z_i)$ represents the probability amplitude of the wave function at position z_i and time t. The numerator computes the weighted sum of positions $z_i(t)$, with the weights given by the probability density $|\Psi(t, z_i)|^2$, while the denominator ensures normalization.

The MSD extends this idea by quantifying the squared deviation of positions over time, specifically relative to the initial position z_0. The MSD is given by:

$$
\begin{aligned}
\text{MSD} &= \frac{\langle \Psi(t) | (\hat{z}(t) - \hat{z}(0))^2 | \Psi(t) \rangle}{\langle \Psi(t) | \Psi(t) \rangle} \\
\\
&= \frac{\sum_i^N (z_i(t) - z_0)^2 |\Psi(t, z_i)|^2}{\sum_i^N |\Psi(t, z_i)|^2}.
\end{aligned}
\tag{7}
$$

This formula calculates the average squared displacement of the wave function from its initial position, weighted by the probability density. MSD can be fitted with:

$$
\text{MSD}_w(t) = D_\beta t^\beta,
\tag{8}
$$

where D_β is a pre-factor and β is the transport exponent.

For diffusive transport, $\beta = 1$, and the MSD follows a linear relationship with time:

$$
\text{MSD} \propto t,
\tag{9}
$$

where D_β in this case becomes the diffusion coefficient here.

This is typical for excitons, which move through molecular systems via short-range hopping. In the case of ballistic transport, where $\beta = 2$, the MSD scales quadratically with time:

$$
\text{MSD} \propto t^2.
\tag{10}
$$

In the context of wave mechanics, a wave packet can be defined as a localized grouping of waves, which is typically formed by the superposition of multiple waves with varying wavelengths and frequencies. In contrast to a continuous wave, which extends indefinitely through space, a wave packet represents a localized disturbance that can be used to describe the motion of a particle or excitation. In many physical systems, the propagation of energy, information, or excitations is described in terms

of wave packets, which represent a fundamental concept in both quantum mechanics and classical wave theory.[35]

A wave packet is constructed by superimposing a range of wave components, each with a distinct wave vector k and angular frequency ω. The overall motion of the wave packet is then governed by how these individual components interfere with each other. In the absence of interactions, the wave packet moves through space, and the speed at which the centre of the packet propagates is called the group velocity.

The group velocity v_g is given by:

$$v_g = \frac{d\omega}{dk},\tag{11}$$

where ω is the angular frequency and k is the wave vector.
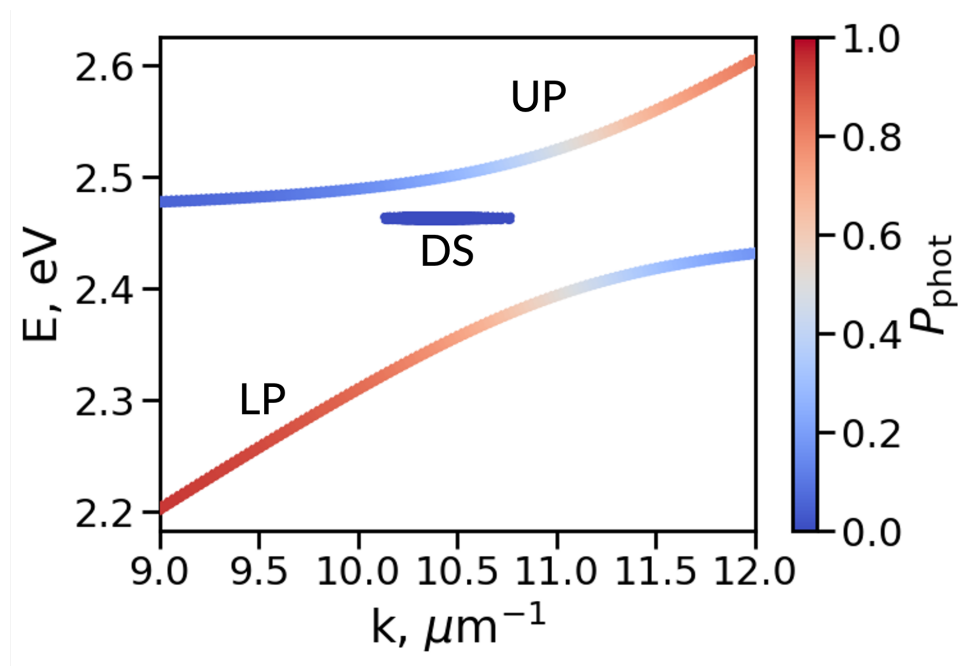

Figure 3. Simulated dispersion of BSW-polaritons structure. The lower polariton (LP) and upper polariton (UP) branches represent the hybridized light-matter states resulting from strong coupling. The dark states (DS) represent uncoupled excitonic states that remain localized and have no contribution from the cavity light modes. The color bar indicates the photonic fraction, P_{phot}, of the polaritonic states, i.e. the total contribution of all cavity modes to each polaritonic state.

Group velocity is crucial in determining polariton transport properties, indicating whether a transport is slow or fast. Figure 3 shows the simulated dispersion for a system with the parameters described in Section 3, revealing two distinct branches formed under strong coupling: the LP and UP. At lower energies, particularly in the wave vector range of $k = 9$ to 9.5 μm^{-1}, the LP branch exhibits a higher photonic weight. Within this range, the group velocity of the LP branch approaches approximately half the speed of light (Figure 4), which is 300 μm/ps, highlighting the significant photonic contribution to polaritonic transport in this region. The

high group velocity serves to illustrate the potential of BSW-polaritons to facilitate efficient, long-distance energy transport, leveraging the low-loss characteristics of BSW structures.
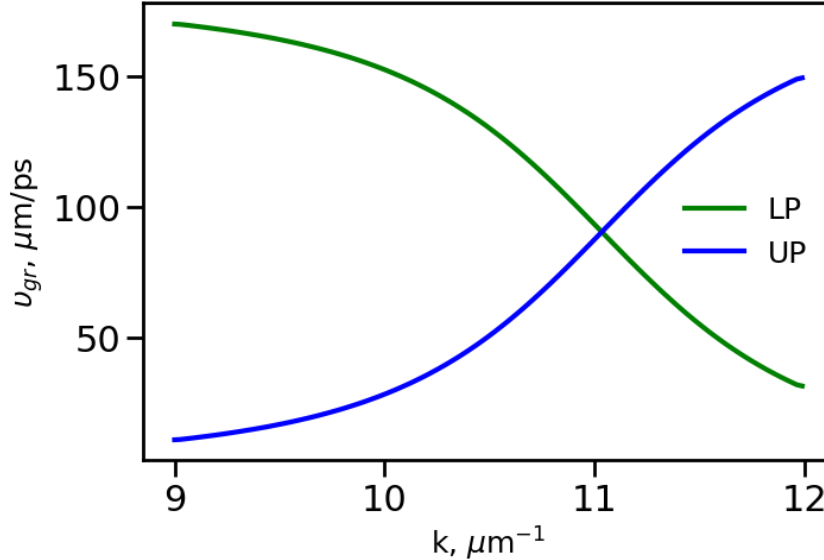

Figure 4. Group velocity of lower (LP, green line) and upper (UP, blue line) BSW-polaritons.

Recently, a study by Balasubrahmaniyam *et al.* have mapped the ultrafast dynamics of polaritons in systems where surface-bound optical waves interact with molecular excitons. The experiments demonstrated a transition between diffusive and ballistic transport, depending on the photonic weight of the LP. Ballistic transport occurs when the photonic component dominates, allowing polaritons to travel over macroscopic distances on the order of 100 micrometers at speeds approaching two-thirds the speed of light and diffusive transport occurs at small photonic contributions.[16]

This shift between transport regimes highlights the flexibility of polaritons as a tool for controlling energy flow in hybrid light-matter systems; however, the reasons behind this have not yet been determined. We have therefore reproduced the experimental part of this article using computers with the aim of gaining a deeper understanding of polariton transport and what causes the crossover in the polariton transport regime.

2.4   Molecular Dynamics Simulations Approach

Molecular Dynamics (MD) simulations, grounded in classical mechanics, provide a microscopic perspective on the behavior of systems by numerically solving Newton's equations of motion. This method enables the study of equilibrium properties, time-dependent phenomena, and the structural evolution of particles on millisecond timescales, offering unmatched insights into molecular interactions and dynamics.[36]

In MD simulations, the system is initialized with particles whose positions and velocities are assigned based on predefined conditions. The positions may follow specific arrangements, such as lattice structures or random distributions, while velocities are typically sampled from the Maxwell-Boltzmann distribution corresponding to the desired temperature.[37] The interactions between particles are described by potential energy functions, known as force fields, which define the forces and energy landscape that govern the system's behavior. These functions include contributions from bonded interactions, such as covalent bonds and angle bending, as well as non-bonded forces like van der Waals and electrostatic interactions.

To compute the time evolution of the system, numerical integration schemes, for example the Verlet or Velocity Verlet algorithms.[38] These methods balance computational efficiency and accuracy, ensuring stable trajectories over extended simulation times. Periodic boundary conditions are often applied to approximate bulk properties and minimize edge effects, where particles leaving one side of the simulation box re-enter from the opposite side, maintaining continuity in the system.

MD simulations typically consist of two phases: equilibration and production. During equilibration, the system evolves toward a steady state, allowing physical properties like temperature and pressure to stabilize around target values. Once equilibrated, the production phase begins, during which trajectories are recorded and time-averaged properties are computed. From these trajectories, key quantities such as radial distribution functions, diffusion coefficients, and root mean square deviation can be extracted, linking molecular-scale dynamics to macroscopic observables through statistical mechanics.

Force fields are crucial to the accuracy of MD simulations. For simple systems, Lennard-Jones potentials effectively capture non-bonded interactions, while more complex systems require sophisticated parameterization that accounts for torsional potentials, long-range electrostatics, and solvent effects.[39] The choice of force field must be validated against experimental data or high-level quantum calculations to ensure reliability.

MD simulations offer valuable insights into molecular behavior and time-dependent processes. However, their reliance on classical Newtonian mechanics inherently limits their ability to accurately capture the quantum nature of molecules, which is important for describing excited states and transition dipole moments. These properties are crucial for understanding light-matter interactions, particularly in the context of strong coupling with cavity modes. The inherent limit restricts the applicability of MD simulations in understanding the mechanisms of complex chemical reactions, emphasizing the need for advanced methods to solve this problem.

2.5 Quantum Mechanics/Molecular Mechanics Approach

In order to overcome the shortcomings of MD simulations, we introduce an advanced method named quantum mechanics/molecular mechanics (QM/MM) approach (Figure.5) , which is based on semi-classical MD simulation, to perform the simulation

of polariton transport.

The QM/MM approach is a hybrid computational approach that allows for the detailed simulation of complex systems where quantum and classical behaviors are intertwined. It is particularly useful for modeling systems where localized quantum interactions, such as those between molecules and confined light fields, are influenced by a broader, classically behaving environment.[40] This approach is essential in situations where full quantum mechanical treatment of the entire system is computationally impractical but where the accuracy of quantum calculations is critical in a specific region of interest.
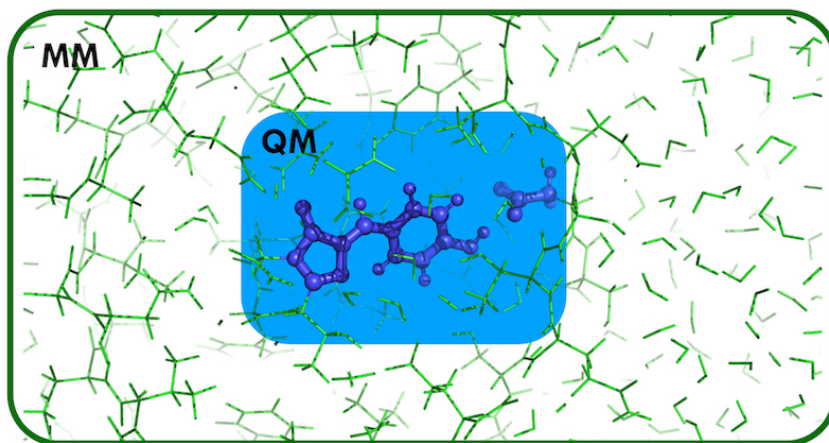

Figure 5. Schematic representation of a QM/MM simulation system.[41] The central region (blue) represents the Quantum Mechanics (QM) region, which contains the molecular system of interest where quantum effects are significant. This region is embedded within the larger Molecular Mechanics (MM) region (green), which models the surrounding environment, using classical mechanics.

In QM/MM approach, the system is partitioned into two regions: the quantum mechanical (QM) region, where quantum effects are important and hence cannot be ignored, and the molecular mechanical (MM) region, which is treated classically. The QM region typically encompasses the part of the system where the chemical reaction or photo-excitation occurs, such as the molecular exciton interacting with the cavity's electromagnetic field.[42] The MM region, on the contrary, models the surrounding environment, such as a solvent or molecular matrix, using classical force fields. This dual treatment is crucial for accurately capturing the quantum properties of large molecules while simultaneously accounting for large-scale environmental effects.

In the context of polaritons, a quantum mechanical description is required to accurately model photoexcitation and light-matter interactions. The QM/MM approach, originally developed to treat quantum effects in molecules while simultaneously capturing the surrounding environment classically, is particularly suited for this purpose. In the context of polariton dynamics, the QM region enables a precise description of the photoexcitation process, which is essential for correctly modeling

light-matter coupling. At the same time, the MM subsystem plays a crucial role in capturing environmental effects such as thermal fluctuations and excitation energy disorder, all of which significantly influence polariton transport. These environmental interactions can modify the transport properties of polaritons by introducing decoherence or altering energy transfer pathways.

By efficiently combining the quantum treatment of light-matter coupling with the classical simulation of the environment, the QM/MM approach provides a powerful framework for studying energy transport in strongly coupled system. This hybrid method is particularly effective in analyzing how confined light interacts with its surroundings, balancing the complexity of quantum interactions with the broader scale of classical systems to enable a realistic investigation of polariton dynamics.

3 Simulation Model

In this chapter, we will focus on the specifics of how to perform semi-classical dynamics simulations within our model. This includes a full explanation of the computational methods used to capture molecular interactions and dynamics and the parameters of the molecules chosen for the simulation.

3.1 Molecular Dynamics Simulation Model

To model the interactions between the molecules and cavity modes, a Multi-scale Tavis-Cummings Hamiltonian[43, 44] (Equation 12) was used. In our MD simulations, we utilize the Born-Oppenheimer approximation[45, 46] to separate the nuclear and electronic-photonic degrees of freedom. The nuclear degrees of freedom are treated classically, while the electronic and photonic degrees of freedom are described quantum mechanically.

$$
\begin{aligned}
\hat{H}^{\mathrm{TC}} \;=\; & \sum_j^N \hbar\omega_{\mathrm{exc}}(\mathbf{R}_j)\hat{\sigma}_j^+\hat{\sigma}_j^- + \sum_{k_z}^{n_{\mathrm{modes}}} \hbar\omega_{\mathrm{cav}}(k_z)\hat{a}_{k_z}^\dagger\hat{a}_{k_z} + \\
& \sum_j^N \sum_{k_z}^{n_{\mathrm{modes}}} \hbar g_j(k_z)\left(\hat{\sigma}_j^+\hat{a}_{k_z}e^{ik_z z_j} + \hat{\sigma}_j^-\hat{a}_{k_z}^\dagger e^{-ik_z z_j}\right) + \\
& \sum_i^N V_{\mathrm{S_0}}^{\mathrm{mol}}(\mathbf{R}_i).
\end{aligned}
\tag{12}
$$

In Equation 12, the operator $\hat{\sigma}_j^+ = |\mathrm{S}_1^j\rangle\langle\mathrm{S}_0^j|$ excites molecule j with nuclear coordinates $\mathbf{R}_j$ from its electronic ground state $|\mathrm{S}_0^j\rangle$, which has an energy $V_{\mathrm{S_0}}(\mathbf{R}_j)$, to its first electronic excited state $|\mathrm{S}_1^j\rangle$, with energy $V_{\mathrm{S_1}}(\mathbf{R}_j)$.

The excitation energy of molecule j, is defined as:

$$
\hbar\omega_{\mathrm{exc}}(\mathbf{R}_j) = V_{\mathrm{S_1}}^{\mathrm{mol}}(\mathbf{R}_j) - V_{\mathrm{S_0}}^{\mathrm{mol}}(\mathbf{R}_j),
\tag{13}
$$

where $V_{\mathrm{S_0}}^{\mathrm{mol}}(\mathbf{R}_j)$ and $V_{\mathrm{S_1}}^{\mathrm{mol}}(\mathbf{R}_j)$ represent the adiabatic potential energy surfaces (PESs) of molecule j in its electronic ground state ($\mathrm{S_0}$) and excited state ($\mathrm{S_1}$), respectively.

Conversely, the operator $\hat{\sigma}_j^- = |\mathrm{S}_0^j\rangle\langle\mathrm{S}_1^j|$ de-excites molecule j from the first electronic excited state $|\mathrm{S}_1^j\rangle$ back to the electronic ground state $|\mathrm{S}_0^j\rangle$.

The last term in Equation 12 is the total potential energy of the system in the absolute ground state (*i.e.*, with all molecules and cavity modes de-excited), defined as the sum of the ground-state potential energies of all molecules in the cavity.

The third term in Equation 12 represents the light-matter interaction under the

long-wavelength and rotating wave approximations:

$$g_j(k_z) = -\boldsymbol{\mu}(\mathbf{R}_j) \cdot \mathbf{u}_{\text{cav}} \cdot |\mathbf{E}|$$

$$= -\boldsymbol{\mu}(\mathbf{R}_j) \cdot \mathbf{u}_{\text{cav}} \sqrt{\frac{\hbar\omega_{\text{cav}}(k_z)}{2\epsilon_0 V_{\text{cav}}}}, \tag{14}$$

where $\boldsymbol{\mu}(\mathbf{R}_j)$ is the transition dipole moment of molecule j, which depends on its molecular geometry $(\mathbf{R}_j)$; $\mathbf{u}_{\text{cav}}$ is the unit vector along the direction of the electric field component of the cavity vacuum field $|\mathbf{E}|$; ϵ_0 is the vacuum permittivity; and V_{cav} is the cavity mode volume.

The electric field distribution in a one-dimensional DBR (Figure 2), or photonic crystal, is governed by the wave equation, where the periodic dielectric constant $\varepsilon(x) = \varepsilon(x + A)$, with period A, determines the behavior of electromagnetic waves[47]

$$\frac{c^2}{\varepsilon(x)}\frac{\partial^2 E(x,t)}{\partial x^2} = -\frac{\partial^2 E(x,t)}{\partial t^2}, \tag{15}$$

where c is the speed of light. By assuming the electric field can be separated into spatial and temporal components, the equation simplifies to an eigenvalue problem that relates the spatial variation of the field to its frequency.

According to the Bloch-Floquet theorem, the solution of the wave equation for the electric field can be expressed as a product of a periodic envelope function and a phase factor, $E_K(x) = u_K(x)e^{iKx}$, where $u_K(x)$ repeats with the periodicity of the structure, and K is the Bloch wave number. For BSW, the Bloch wave number is complex, $K = i|K|$, leading to an exponentially decaying field inside the photonic crystal:

$$E_K(x) = u_K(x)e^{-|K|x}. \tag{16}$$

Therefore, the electric field strength of the BSW exhibits a periodic decay inside the photonic crystal (indicated by the black line at $x < 0$ in Figure 2). In the air, outside the photonic crystal, the periodic modulation of the dielectric constant is absent, and the electric field decays purely exponentially as:

$$E_K(x) = E_0 e^{-|K|x}, \tag{17}$$

where E_0 represents the electric field strength at the interface between the photonic crystal and air.

It is worth mentioning that the electric field of the BSW along the DBR surface can propagate freely as a plane wave along the entire yz surface. In this work, we restrict ourselves to modelling the one-dimensional transport along a molecular chains (orange ellipses in Figure 2) in the z direction:

$$E(z) = E_0 e^{ik_z z}. \tag{18}$$

Following Michetti and La Rocca,[48] we introduce periodic boundary conditions along the z-direction of the DBR to limit the wave vectors to discrete values: $k_{z,p} = 2\pi p/L_z$, where $p \in \mathbb{Z}$ and L_z is the DBR slab width. Therefore, the Tavis-Cummings Hamiltonian in (Equation 12) can be represented as a matrix with four blocks,

$$\mathbf{H}^{\mathrm{TC}} = \begin{pmatrix} \mathbf{H}^{\mathrm{mol}} & \mathbf{H}^{\mathrm{int}} \\ \mathbf{H}^{\mathrm{int}\dagger} & \mathbf{H}^{\mathrm{cav}} \end{pmatrix}. \tag{19}$$

The upper left block, $\mathbf{H}^{\mathrm{mol}}$, is a $N \times N$ matrix containing the single-photon excitations of the molecules. Since direct exciton interactions between molecules are ignored, the block is diagonal. Each matrix element of $\mathbf{H}^{\mathrm{mol}}$ represents the potential energy of molecule j for $1 \le j \le N$ in the electronic excited state $|S_1^j(\mathbf{R}_j)\rangle$ and all other molecules $i \ne j$ in the electronic ground states $|S_0^i(\mathbf{R}_i)\rangle$.

$$H_{j,j}^{\mathrm{mol}} = V_{\mathrm{S}_1}^{\mathrm{mol}}(\mathbf{R}_j) + \sum_{i \ne j}^{N} V_{\mathrm{S}_0}^{\mathrm{mol}}(\mathbf{R}_i). \tag{20}$$

The lower right block, $\mathbf{H}^{\mathrm{cav}}$, is a $n_{\mathrm{modes}} \times n_{\mathrm{modes}}$ matrix (with $n_{\mathrm{modes}} = n_{\mathrm{max}} - n_{\mathrm{min}} + 1$) containing the single-photon excitations of the cavity modes. Each matrix element of $\mathbf{H}^{\mathrm{cav}}$ represents the energy which is the sum of ground state energies of all molecules and the energy of cavity mode p for $0 \le p \le n_{\mathrm{max}}$ in the excited state with wave vector $k_{z,p} = 2\pi p/L_z$.

$$H_{p,p}^{\mathrm{cav}} = \hbar\omega_{\mathrm{cav}}\left(2\pi p/L_z\right) + \sum_j^{N} V_{\mathrm{S}_0}^{\mathrm{mol}}(\mathbf{R}_j), \tag{21}$$

where $\omega_{\mathrm{cav}}(2\pi p/L_z)$ is the cavity dispersion, and in this project the dispersion of the BSW is fitted to reproduce the experimental dispersion.[16]

The two $N \times n_{\mathrm{modes}}$ off-diagonal blocks $\mathbf{H}^{\mathrm{int}}$ and $\mathbf{H}^{\mathrm{int}\dagger}$ represent the interactions between the molecules and the cavity modes. These matrix elements are approximated based on the overlap between the transition dipole moment of the molecule j between its ground state and first excited state and the electric field of the cavity mode p,

$$
\begin{aligned}
H_{j,p}^{\mathrm{int}} &= -\boldsymbol{\mu}(\mathbf{R}_j) \cdot \mathbf{u}_{\mathrm{cav}} \sqrt{\frac{\hbar\omega_{\mathrm{cav}}(2\pi p/L_z)}{2\epsilon_0 V_{\mathrm{cav}}}} \langle\phi_0|\hat{\sigma}_j\hat{\sigma}_j^+ \hat{a}_p e^{i2\pi pz_j/L_z} \hat{a}_p^\dagger|\phi_0\rangle \\
&= -\boldsymbol{\mu}(\mathbf{R}_j) \cdot \mathbf{u}_{\mathrm{cav}} \sqrt{\frac{\hbar\omega_{\mathrm{cav}}(2\pi p/L_z)}{2\epsilon_0 V_{\mathrm{cav}}}} e^{i2\pi pz_j/L_z}
\end{aligned}
\tag{22}
$$

for $1 \le j \le N$ and $n_{\mathrm{min}} \le p \le n_{\mathrm{max}}$.

The Ehrenfest molecular dynamics method was employed to describe the evolution of the classical degrees of freedom.[49] In this approach, the classical coordinates evolve on a potential energy surface defined as the expectation value of the total energy of the quantum wave function: $V(\mathbf{R}) = \langle\Psi|\hat{H}|\Psi\rangle$. The total wave function, $|\Psi(t)\rangle$, was propagated along the classical trajectory as a linear combination of diabatic product states involving the N molecular excitations and the n_{modes} BSW modes:[50]

$$|\Psi(t)\rangle = \sum_{j}^{N+n_{\mathrm{modes}}} d_j(t)|\phi_j\rangle, \tag{23}$$

with

$$|\phi_j\rangle = \hat{\sigma}_j^+ |S_0^1 S_0^2 .. S_0^{N-1} S_0^N\rangle \otimes |00..0\rangle \tag{24}$$

for $1 \leq j \leq N$, and

$$|\phi_{j>N}\rangle = \hat{a}_{j-N}^\dagger |S_0^1 S_0^2 .. S_0^{N-1} S_0^N\rangle \otimes |00..0\rangle \tag{25}$$

for $N < j \leq N + n_{\text{modes}}$.

The state $|\phi_j\rangle$ represents molecule j in its first electronic excited state (S_1^j), while all other molecules remain in their ground states ($S_0^{i \neq j}$) and the photonic modes are unoccupied. Conversely, the state $|\phi_{j>N}\rangle$ corresponds to one of the BSW modes being excited, with all molecules in their electronic ground states. In Equation 23, the coefficients $d_j(t)$ are time-dependent expansion coefficients of the total wave function, representing the population of each molecular excitation and photonic mode as the system evolves. These coefficients were propagated using a unitary propagator.[51]

In order to analyse the trajectories, we also expand the total time-dependent wave function in the basis of the eigenstates of the Tavis-Cummings Hamiltonian, as follows:

$$|\Psi(t)\rangle = \sum_j c_m(t)|\psi_m\rangle, \tag{26}$$

where

$$|\psi_m\rangle = \left(\sum_j^N \beta_j^m \hat{\sigma}_j^+ + \sum_p^{n_{\text{modes}}} \alpha_p^m \hat{a}_p^\dagger \right) |S_0^1 S_0^2 .. S_0^{N-1} S_0^N\rangle \otimes |0\rangle. \tag{27}$$

In this context, the expansion coefficients β_j^m and α_p^m represent the contributions of molecular excitons ($|S_1^j\rangle$) and photonic modes ($|1_p\rangle$) to the adiabatic eigenstate $|\psi_m\rangle$. These coefficients are determined by diagonalizing the matrix representation of $\hat{H}^{\text{TC}}$ (Equation 19) in the basis of diabatic product states (Equations 24-25). The time-dependent expansion coefficients $c_m(t)$ in the adiabatic representation are related to the time-dependent coefficients $d_j(t)$ in the diabatic representation (Equation 23) through the unitary matrix $\mathbf{U}$, which diagonalizes the Tavis-Cummings matrix. Specifically, this relationship is given by

$$c_m(t) = \sum_j^{N+n_{\text{modes}}} U_{mj}^\dagger d_j(t), \tag{28}$$

where $U_{jm} = \beta_j^m$ if $j \leq N$ and $U_{jm} = \alpha_{j-N}^m$ if $j > N$.

To investigate the influence of the photonic properties of the adiabatic eigenstates on their contribution to overall transport, the photonic part of the total wave function was decomposed into *partial* wave functions within a window w of width Δk_z defined as:

$$|\Psi_{\text{phot},w}^{\text{part}}(z_j, t)\rangle = \frac{1}{\sqrt{N}} \sum_{m' \in w}^{n_{\text{modes}}} c_{m'}(t) \sum_p^{n_{\text{modes}}} \alpha_p^{m'} e^{ik_{z,p} z_j} \hat{a}_p^\dagger |\phi_0\rangle, \tag{29}$$

where z_j is the position of molecule j (with $z_j = (j-1)L_z/N$ for $1 \leq j \leq N$).

These partial wave functions are linear combinations of the eigenstates of the Tavis-Cummings Hamiltonian (Equation 27) corresponding to fixed wave vector intervals, referred to as windows, w_i. Each window is centered at $k_{z,i}$ and spans the range from $k_{z,i}^{\min}$ to $k_{z,i}^{\max}$. The expansion coefficients $c_{m \in w_i}(t)$ for these partial wave functions are determined by projecting the adiabatic eigenstates within a given window onto the total time-dependent wave function in the adiabatic representation (Equation 26).

3.2 Methylene Blue Model

In order to study the experimentally observed shifts in polariton transport modes, QM/MM molecular dynamics simulations were conducted for a system of $N = 1024$ methylene blue (MeB, Figure 6) molecules in water, coupled to a BSW.

MeB molecules were chosen for the simulations instead of the experimentally[16] used J-aggregates due to the latter's complexity, which currently renders their simulation in a cavity computationally prohibitive. Despite having a broader absorption line-width, MeB molecules retain the key characteristics of J-aggregates, including a bright electronic transition and several Raman-active vibrational modes,[52] making them suitable substitutes for the study.
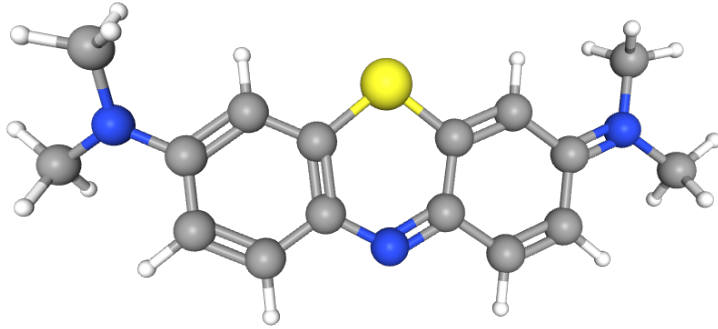

Figure 6. Molecular structure of Methylene Blue (MeB) molecule.[53]The grey spheres represent carbon atoms, blue spheres indicate nitrogen atoms, yellow represents a sulfur atom, and white spheres correspond to hydrogen atoms.

To model the MeB-BSW system, the electronic ground state (S_0) and first excited state (S_1) of MeB were described using density functional theory (DFT) and time-dependent density functional theory (TDDFT) with the B97 functional and 3-21G basis set.[54,55,56,57] The interactions between MeB and the water solvent were modeled using the Amber03 force field, while water molecules were represented by

the TIP3P model.[58] Partial atomic charges for MeB were derived using the RESP method[59] based on electrostatic potential calculations obtained from geometry optimizations at the HF/6-31G** level, employing the IEFPCM continuum solvent model.[60]

The simulation box contained one MeB molecule, initially optimized at the B97/3-21G level, and 2031 TIP3P water molecules. Van der Waals interactions were modeled using Lennard-Jones potentials, while Coulomb interactions were computed using the particle mesh Ewald method.[61] The system was equilibrated at 300 K and 1 atm with a 2 fs timestep using the v-rescale thermostat[62] and the Berendsen pressure coupling algorithm[63]. Subsequently, the system underwent QM/MM equilibration, treating MeB quantum mechanically while representing water classically. At this level of theory, the excitation energy of MeB was determined to be 2.5 eV, which is shifted with respect to experimentally measured excited state of MeB at 1.86 eV,[64] but can be compensated by tuning the cavity resonance.

To replicate the initial conditions of the experiment,[16] where a single J-aggregate was optically pumped, the system was initialized with a single MeB molecule, j, excited to the S_1 state at $z_j = 125$ μm. This corresponds to $d_j(0) = 1$ and $d_{i \neq j}(0) = 0$ in Equation 23, placing the excitation at the center of a periodic DBR surface of width $L_z = 250$ μm. BSW modes were discretized into 120 components to simulate the polariton dispersion. The experimental BSW dispersion was fit to a linear function, $E_{\mathrm{BSW}}(k_z) = 0.119 \cdot k_z + 0.771$ eV, and adjusted to match the MeB excitation energy.[16]

Simulations were conducted using five Ehrenfest QM/MM trajectories for 200 fs with a 0.5 fs timestep. Decay effects were neglected due to the short trajectory times compared to the typical BSW lifetime.[65] The vacuum electric field was set to 0.071 MV/cm, resulting in a Rabi splitting of 131 meV, which closely matches the experimental value of 142 meV. Partial wave functions were analyzed across different wave vector windows to investigate polariton transport along the LP branch.

4 Polariton Transport in BSW Structure

In this chapter, the results of polariton transport simulations are presented, accompanied by an analysis and discussion of the results. In Section 4.1, static two-level simulations with excitation energy disorder are performed to determine whether the experimentally observed shift can be explained by it. Then molecular simulations with dynamic factors are performed in Section 4.2. In order to better analyze the LP states with different ranges of wave vectors, in Section 4.3 we introduce the concept of windows. Thus, we are able to study the regime of polariton transport in the seven windows. The results of static two-level systems and molecular dynamics simulation models using the window strategy, are respectively presented in subsections 4.3.1 and subsections 4.3.2. Together, this chapter provides a theoretical basis for exploring the experimentally observed shift from ballistic to diffusive.

4.1 Static Two-Level Model

To establish a foundation for investigating polariton transport dynamics, we first performed simulations of $N = 1000$ static two-level systems before conducting MD simulations of realistic molecules. The two-level model is computationally cheap and isolates the essential physical interactions, capturing the hybridization between excitons and cavity modes that results in strong coupling. This approach allows for rapid testing and tuning of key parameters, such as exciton-cavity resonance and Rabi splitting, which are critical for ensuring a strong coupling regime. Additionally, the two-level model provides a benchmark for validating the polariton dispersion against experimental results, ensuring consistency before transitioning to more complex simulations incorporating environmental effects and dynamic molecular interactions.

The comparison of simulated (Figure 7a) and experimental (Figure 7b) dispersions of the BSW polaritons demonstrates the consistency between the theoretical model and experimental observations. In Figure 7a, the dispersion is characterized by the LP and UP branches, with the photonic weight (P_{phot}) indicated by the color gradient. At smaller wave vectors, the LP branch becomes more photonic, resulting in a greater group velocity (Figure 4). The black dashed line in Figure 7a was taken from the experimental LP data (dotted line) shown in Figure 7b, highlighting the agreement between simulation and experiment. The black line in Figure 7a is a linear fit to the experimental dispersion of the BSW[16] (which corresponds to the white line in Figure 7b), with linear function $E_{\text{BSW}}(k_z) = a \cdot k_z + b$ with $a = 0.119$ eVμm^{-1} and $b = 0.771$ eV. In Figure 7b, the white horizontal line represents the excitation
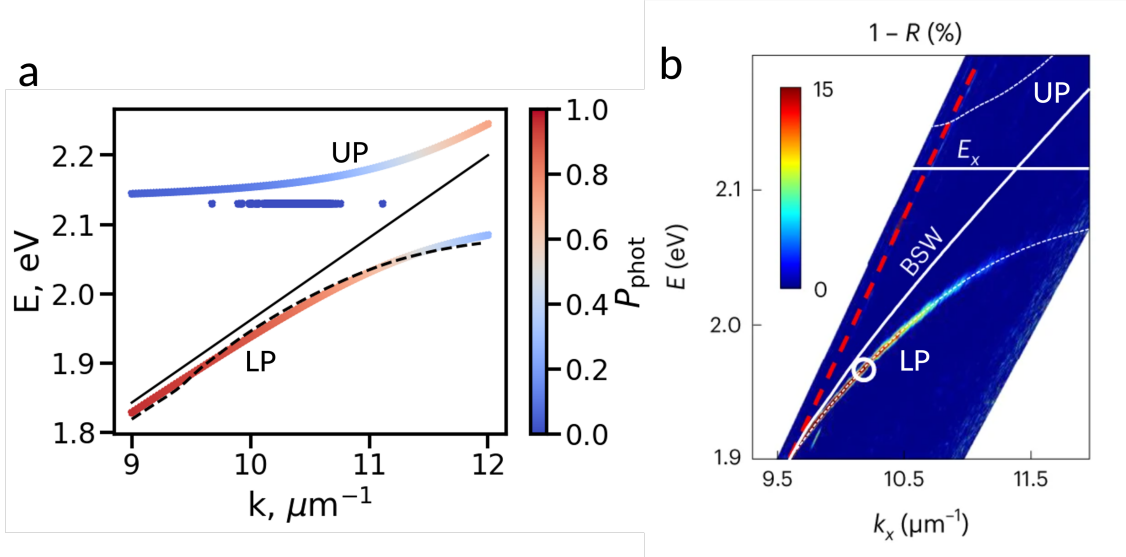
Figure 7. Dispersion of BSW-polaritons from simulation (panel **a**) and the experiment (panel **b**). In Panel **a**, dispersion of the BSW is shown as the black line, the dashed line is experimental data corresponding to the LP line (dotted line) in panel **b**. Panel **b** is reproduced with permission from Balasubrahmaniyam *et al.*, *Nat. Mater.*, **22**, 338-344 (2023). Copyright 2023 Springer Nature Ltd.

energy (E_x) of a J-aggregate of cyanine dyes used in the experimental study, which was selected as the initial configuration for each of $N = 1024$ two-level systems in static simulations.

This alignment between the simulated and experimental LP dispersions underscores the reliability of the two-level model for accurately describing the hybridization of light and matter. It validates the use of this model for further exploration of polariton transport dynamics.

In the simulation of static two-level systems, we also introduce an excitation energy disorder, which is derived from a Gaussian distribution, which is defined as:

$$p(E) = \frac{1}{\sqrt{2\pi}\sigma} \exp\left[-\frac{(E - E_0)^2}{2\sigma^2}\right],$$ (30)

where E_0 is the mean value, and σ is the *disorder strength* that determines the absorption line-width of the disordered two-level system.

The time-space maps presented in Figure 8 illustrate the evolution of the total polariton wave function probability amplitude, $|\Psi(z,t)|^2$, under two different conditions: without static excitation energy disorder (Figure 8a) and with static excitation energy disorder (Figure 8b). The color scale illustrates the logarithmic amplitude of the probability density, where higher intensities correspond to regions of significant wave function presence. In Figure 8a, where no static excitation energy disorder is introduced, the initial excitation at $z \approx 125$ μm generates a wave packet that propagates coherently along the z-axis over time. The propagation is predominantly directional, with the wave packet spreading smoothly, contributed by

polaritonic states propagating ballistically with their group velocities according to the polariton dispersion (Figure 7a and 4). The amplitude decreases uniformly with time as the wave packet disperses across a larger spatial region, reflecting a well-preserved coherence. The continuous and smooth distribution of the wave packet highlights the efficient energy transfer facilitated by strong coupling in the absence of external perturbations.
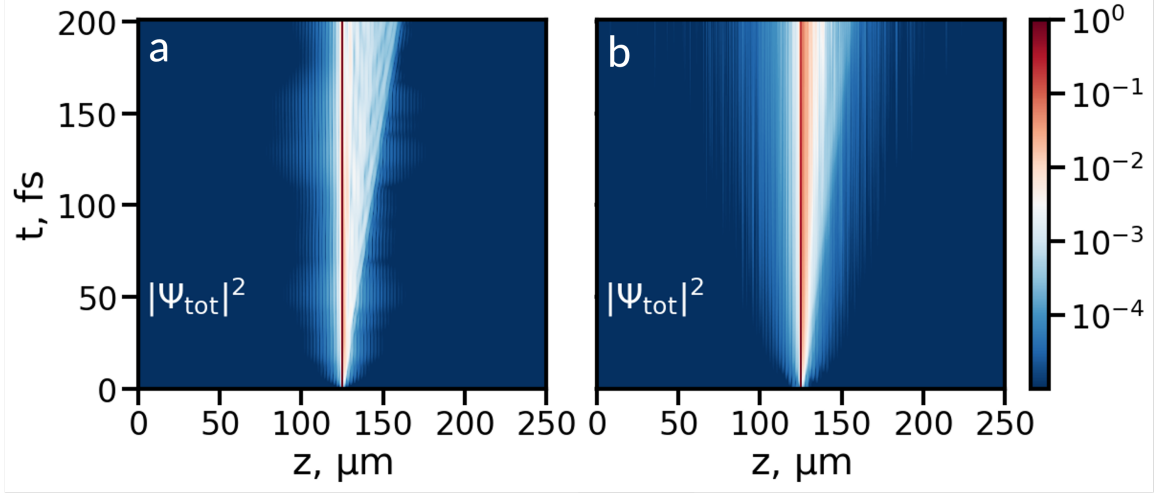

Figure 8. Time-space maps of the probability amplitude of the total wave function $|\Psi(z,t)|^2$, without (panel **a**) and with static excitation energy disorder (panel **b**). Panel **b** is an average over 100 realisations of disorder.

In contrast, Figure 8b shows the propagation dynamics when static excitation energy disorder is introduced into the system. Although the initial excitation is similarly localized at $z \approx 125$ μm, the subsequent propagation of the wave packet is visibly disrupted. A significant portion of the probability amplitude remains near the initial excitation site, suggesting that static excitation energy disorder introduces localization effects and hinders long-range transport. The wave packet becomes fragmented, with irregular bands of intensity indicating scattering and reduced coherence. Unlike the directional uniform spreading observed in Figure 8a, the presence of disorder leads to a more diffusive transport regime, characterized by diminished propagation and weakened spatial coherence.

4.2 Molecular Dynamic Simulations

As in previous section, in the MD simulations, we analyze the time-space evolution of the probability amplitude of the total wave function, $|\Psi(z,t)|^2$. Figure 9 depicts the spatial and temporal distribution of a polariton wave packet after excitation at $z = 125\,\mu$m. The wave function begins at the excitation point and propagates along the z-axis, demonstrating ballistic transport behavior over the simulated timescale of 200 femtoseconds. This result highlights the coherent propagation of the polaritonic wave packet within the system, a key feature of strong light-matter coupling.
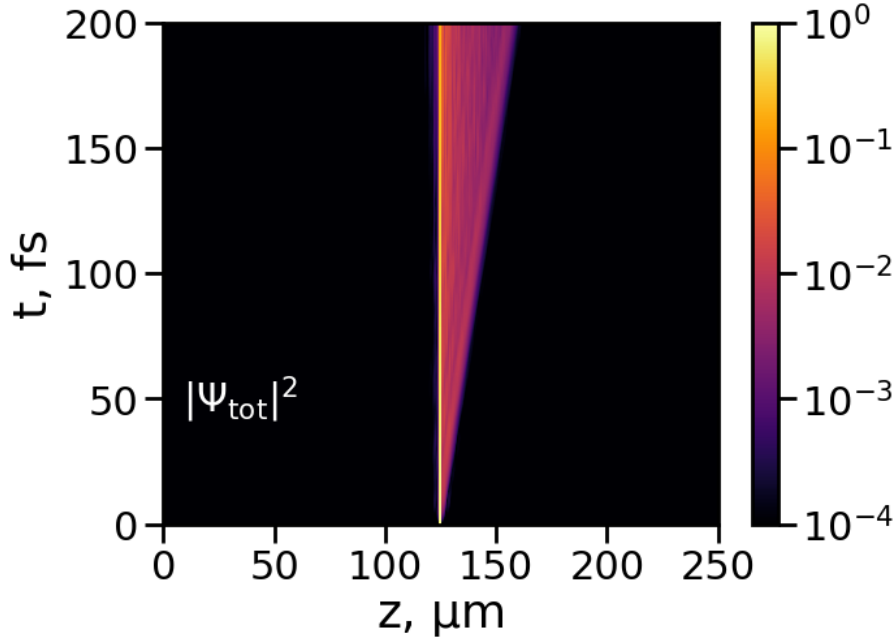

Figure 9. Time-space map of the probability amplitude of the total wave function, $|\Psi(z,t)|^2$.

Figure 10 illustrates the mean squared displacement, $\mathrm{MSD}_w(t) - \mathrm{MSD}_w(0)$, of the total wave function $|\Psi(z,t)|^2$ as a function of time. The MSD increases steadily, and the excellent agreement with a quadratic fit (dashed line in Figure 10) implies ballistic transport of the polariton wave packet.

Figure 11a illustrates the dispersion obtained from the static model without excitation energy disorder, while Figure 11b presents the results from MD simulations. In the static model, the LP branch displays a consistent, gradual change of photonic contribution (P_{phot}) across the wave vectors, reflecting the behavior expected in an ideal system without energy disorder. This uniformity suggests a relatively wide distribution of bright polaritonic states with well-defined wave vectors.

In contrast, the MD simulations (Figure 11b) reveal significant disruption in the dispersion profile. The inclusion of energy disorder in these simulations leads to scattering of the polaritonic states, especially in the DS region, leading to irregular P_{phot} distribution. Consequently, the range of bright polaritonic states is reduced, effectively narrowing the LP branch and highlighting the impact of disorder on
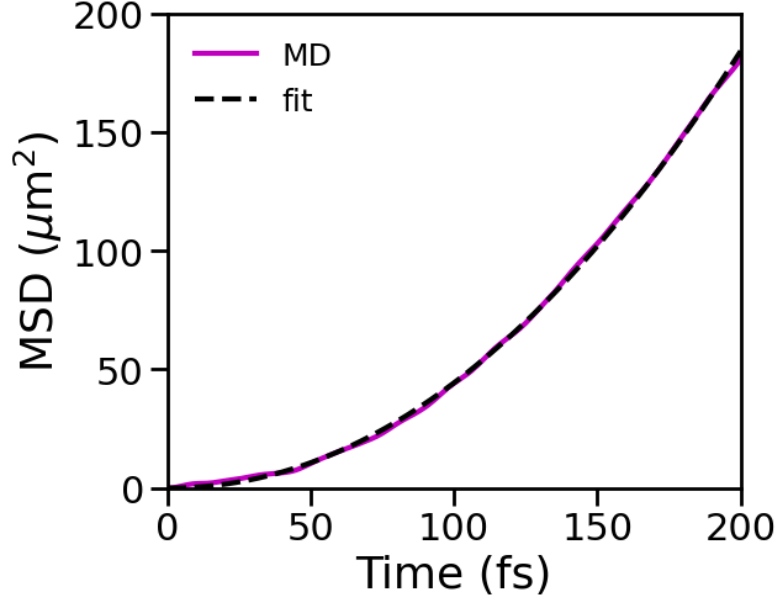
Figure 10. Mean squared displacement, $\text{MSD}_w(t) - \text{MSD}_w(0)$, of the total wave function $|\Psi|^2$ as a function of time. The dashed line is a fit to a quadratic function (Equation 8).

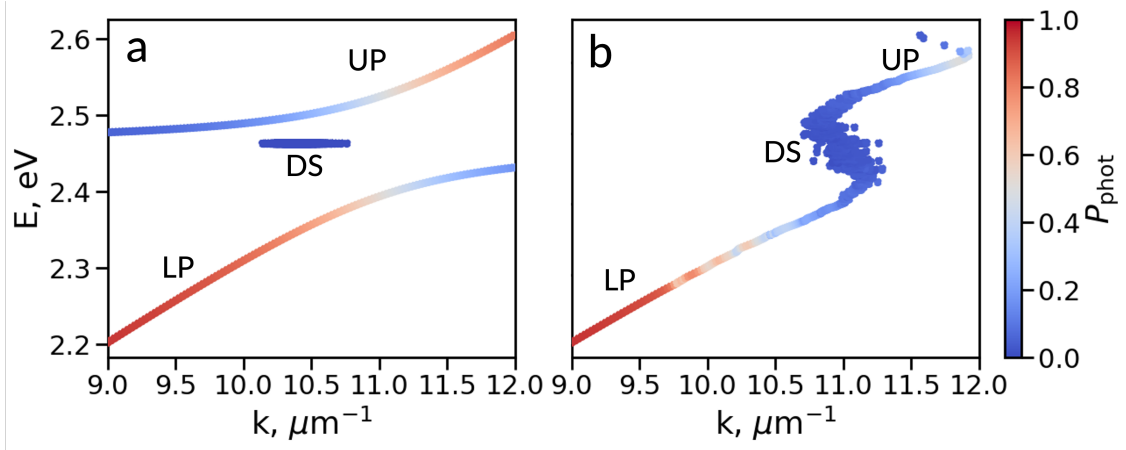Figure 11. Panel **a**: Simulated dispersion of BSW-polaritons with static two-level model without excitation energy disorder. Panel **b**: Simulated dispersion of BSW-polaritons with MD model for a single instant of time.

polariton coherence. This comparison demonstrates how energy disorder modifies the dispersion, diminishing both the clarity and the range of wave vectors associated with well-defined polaritonic states.[66]

4.3 Resolving Polariton Transport in Energy/Momentum Space

To analyze how different LP states with specific wave vectors contribute to the overall propagation of the total wave function, we divided the dispersion into discrete wave vector intervals, referred to as windows (w), as depicted in Figure 12. Since the photonic component of the wave function is less affected by fluctuations in molecular excitation energies compared to the total or excitonic wave functions,[20] therefore, for each window, we constructed partial *photonic* wave functions ($|\Psi^{\text{part}}_{\text{phot},w}(z,t)\rangle$, Equation 29). Each window corresponds to a fixed range of wave vectors, as listed in Table 1. These partial *photonic* wave functions capture the contributions of LP states within their respective wave vector ranges.
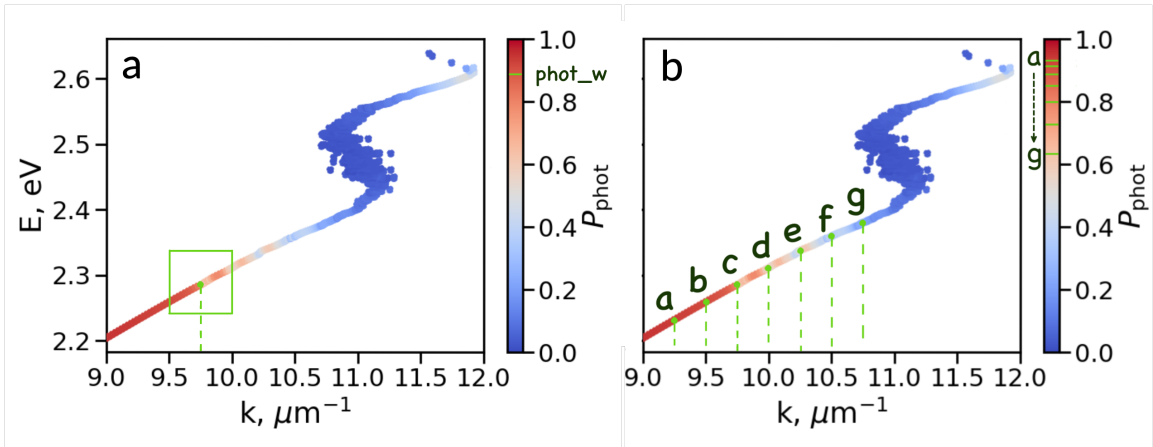

Figure 12. Polariton dispersion in molecular dynamics simulations at time t=0. Green frame in panel **a** shows one of the wave vector windows through which partial photonic wave functions, $|\Psi^{\text{part}}_{\text{phot},w}|^2$, was extracted. Panel **b** indicates the positions of the centre of each of seven windows (Table 1), through which partial photonic wave function was extracted.

The central position of each window (k_z^c) represents the wave vector corresponding to the middle of the interval, for which the total photonic contribution of the BSW modes is $|\alpha_m^c|^2$ (third column in Table 1). For example, in window a ($k_z \in [9.00, 9.50]$ μm^{-1}), the central wave vector is $k_z^c = 9.25$ μm^{-1}, with a corresponding photonic contribution of $|\alpha_m^c|^2 = 0.93$, suggesting that this state is predominantly photonic. As the wave vector increases across the windows (e.g., from window a to window g), the photonic character gradually decreases, indicating a transition to the more excitonic character.

This windowing strategy is essential to distinguish the contributions of polaritonic states across the LP branch and to observe how the wave packet dynamics vary with changes in the photonic-to-excitonic character. By extracting partial wave functions from these windows, we are able to analyze the time evolution of the probability densities ($|\Psi^{\text{part}}_w(z,t)|^2$), shown in subsequent subsections, and gain

Table 1. Ranges of wave vectors (k_z, first column) at which partial photonic wave functions, $|\Psi_{\text{phot}}^{\text{part}}(z,t)\rangle$, were extracted. The third and fourth columns indicate, respectively, the wave vector of the polariton state corresponding to the centre of each window (k_z^c) and the total contribution of all BSW modes ($|\alpha_m^c|^2 = \sum_p^{n_{\text{modes}}} |\alpha_p^m|^2$) to this state.

Index letter	k_z-range (μm^{-1})	k_z^c (μm^{-1})	$|\alpha_m^c|^2$
a	[9.00; 9.50]	9.25	0.93
b	[9.25; 9.75]	9.50	0.91
c	[9.50; 10.00]	9.75	0.89
d	[9.75; 10.25]	10.00	0.85
e	[10.00; 10.50]	10.25	0.80
f	[10.25; 10.75]	10.50	0.73
g	[10.50; 11.00]	10.75	0.64

insight into the transport characteristics of the LP states at different wave vector regions.

4.3.1 Simulation of Two-Level Systems with Static Excitation Energy Disorder

To investigate whether the transition from ballistic to diffusive transport along the LP branch can be attributed solely to the excitation energy disorder, we performed simulations involving $N = 1000$ statically disordered two-level systems. In these simulations, the excitation energies of the two-level systems were drawn from a Gaussian distribution (Equation 30).

The MSD$_w$ of the partial *photonic* wave function $|\Psi_{\text{phot}}^{\text{part}}|^2$ is shown for different wave vector windows in static simulations, both without (Figure 13a) and with excitation energy disorder (Figure 13b, $\sigma = 63$ meV). In the absence of disorder, the MSD curves exhibit a parabolic increase over time, characteristic of ballistic transport. Notably, as the wave vector window shifts toward higher values (from $k \in [9.0; 9.5]$ μm^{-1} to $k \in [10.5; 11.0]$ μm^{-1}), the MSD growth rate decreases. This reduction reflects the diminishing group velocity of polariton states at higher wave vectors (Figure 4), where the photonic component of the polariton wave function decreases.[67,68]

When static excitation energy disorder is introduced (Figure 13b), the MSD curves retain their parabolic shape, indicating that polariton propagation remains ballistic despite the disorder. While there is a slight reduction in the overall MSD growth compared to the disorder-free case, particularly for higher wave vector windows, the persistence of ballistic behavior demonstrates that static excitation energy disorder alone is insufficient to explain the experimentally observed transition to diffusive transport, at least for short time-scales simulated in this work.
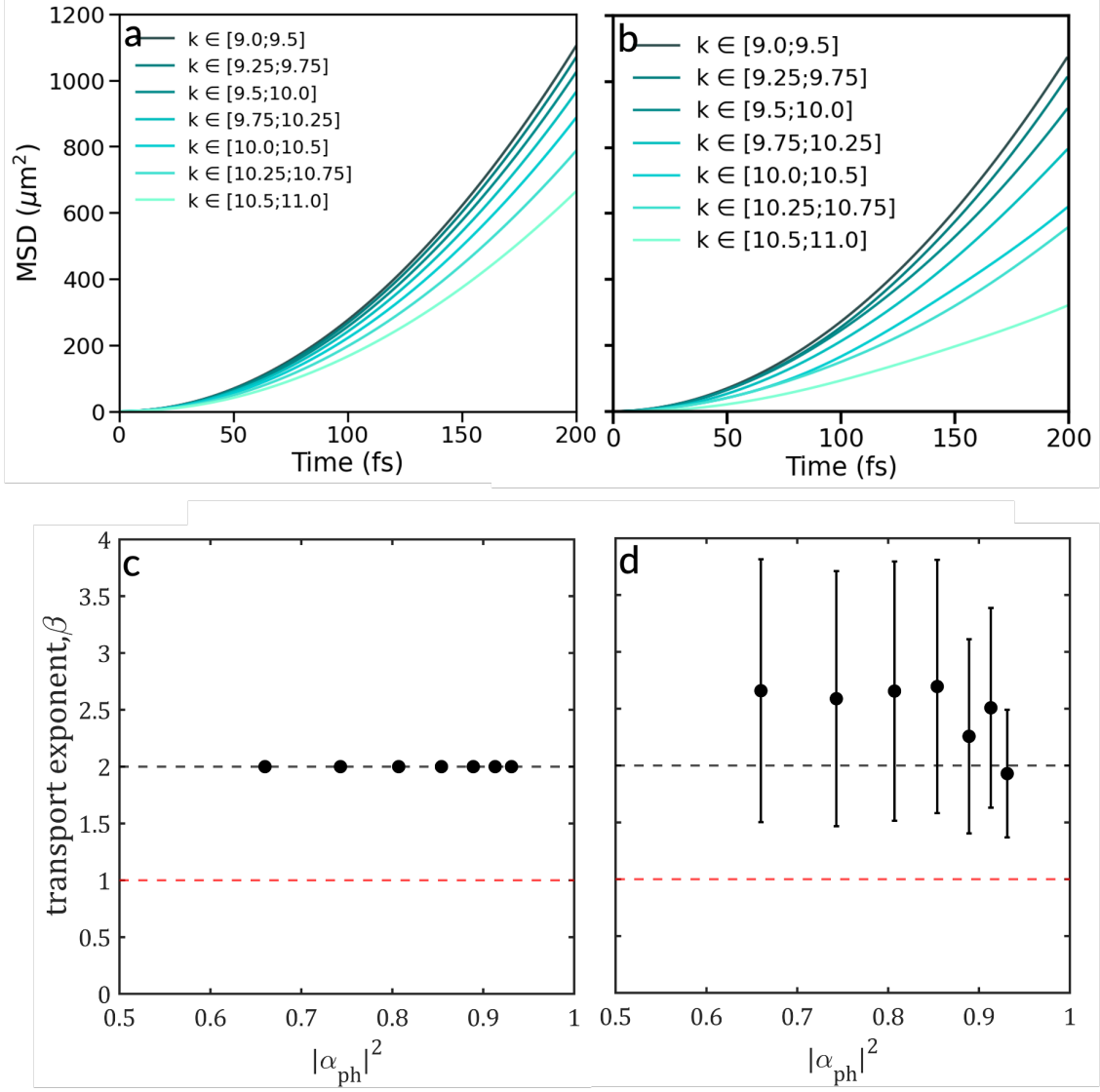
Figure 13. Panels **a** and **b**: Mean squared displacement (MSD$_w$) of the partial photonic wave function $|\Psi_{\text{phot}}^{\text{part}}|^2$ extracted from different wave vector windows in static simulations of two-level systems without ($\sigma = 0$ meV, **a**) and with ($\sigma = 63$ meV, **b**) excitation energy disorder. Panels **c** and **d**: Values of the transport exponent, β, as a function of the BSW modes contribution $|\alpha_{\text{ph}}|^2$ to polaritonic states. The errors are standard deviations of five hundred individual runs.

After fitting the MSD to the Equation 8 (see Table 2 for the values of a regression coefficient), the transport exponents β can be extracted. Figure 13**c**-**d** displays β as a function of the photonic contribution $|\alpha_{\text{ph}}|^2$ to the polaritonic states. All of the extracted values of β remain close to 2, reflecting the characteristic of ballistic motion, no matter the excitation energy disorder is included or not.

Table 2. Coefficients of determination (R^2) for the fits to Expression 8 of the MSD_w's obtained for the partial photonic wave function, $|\Psi_{\text{phot},w}^{\text{part}}(z,t)\rangle$, in static simulations of two-level systems with disorder strength σ of 63 meV . The first column indicates ranges of wave vectors (k_z) at which partial wave functions were extracted. The second column shows the corresponding coefficients of determination.

k_z-range (μm^{-1})	R^2 ($\sigma = 63$ meV)
$[9.00; 9.50]$	1.0000
$[9.25; 9.75]$	0.9998
$[9.50; 10.00]$	0.9986
$[9.75; 10.25]$	0.9986
$[10.00; 10.50]$	0.9983
$[10.25; 10.75]$	0.9998
$[10.50; 11.00]$	0.9989

However, this result deviates from experimental observations, which suggest a transition from ballistic to diffusive polariton transport. This discrepancy highlights the limitations of the static model: while it succeeds in capturing the idealised behaviour of the system, it fails to take into account realistic environmental effects such as dynamic disorder and molecular vibrations, which play a crucial role in modifying polariton transport.[69, 70] As a result, the purely ballistic transport predicted by the static model is not consistent with the dynamics observed experimentally, and more advanced simulations are needed to incorporate these environmental factors.

4.3.2 Transition from Ballistic to Diffusive Motion in MD Simulations

Figure 14**a**-**g** shows the time-space maps of the probability amplitude of the partial *photonic* wave function $|\Psi_{\text{phot}}^{\text{part}}(z,t)|^2$ in different wave vector windows in a system of $N = 1024$ MeB molecules. These maps reveal how the photonic component of the polariton state propagates within these intervals. Polariton wave packets in lower k_z windows (e.g., Figure 14**a** and Figure 14**b**) exhibit stronger spatial propagation, owing to a higher photonic contribution of the states within these windows.

In Figure 14**h**, P_{phot} systematically decreases with increasing k_z value, which directly affects the propagation of the observed polariton dynamics in the time-space maps. As a result of an increase in the excitonic content of polariton states at higher k_z values, such as in Figure 14**f** and Figure 14**g**, polariton wave packets in these windows undergo a stronger scattering and propagate slower than the wave packets at lower k_z windows.
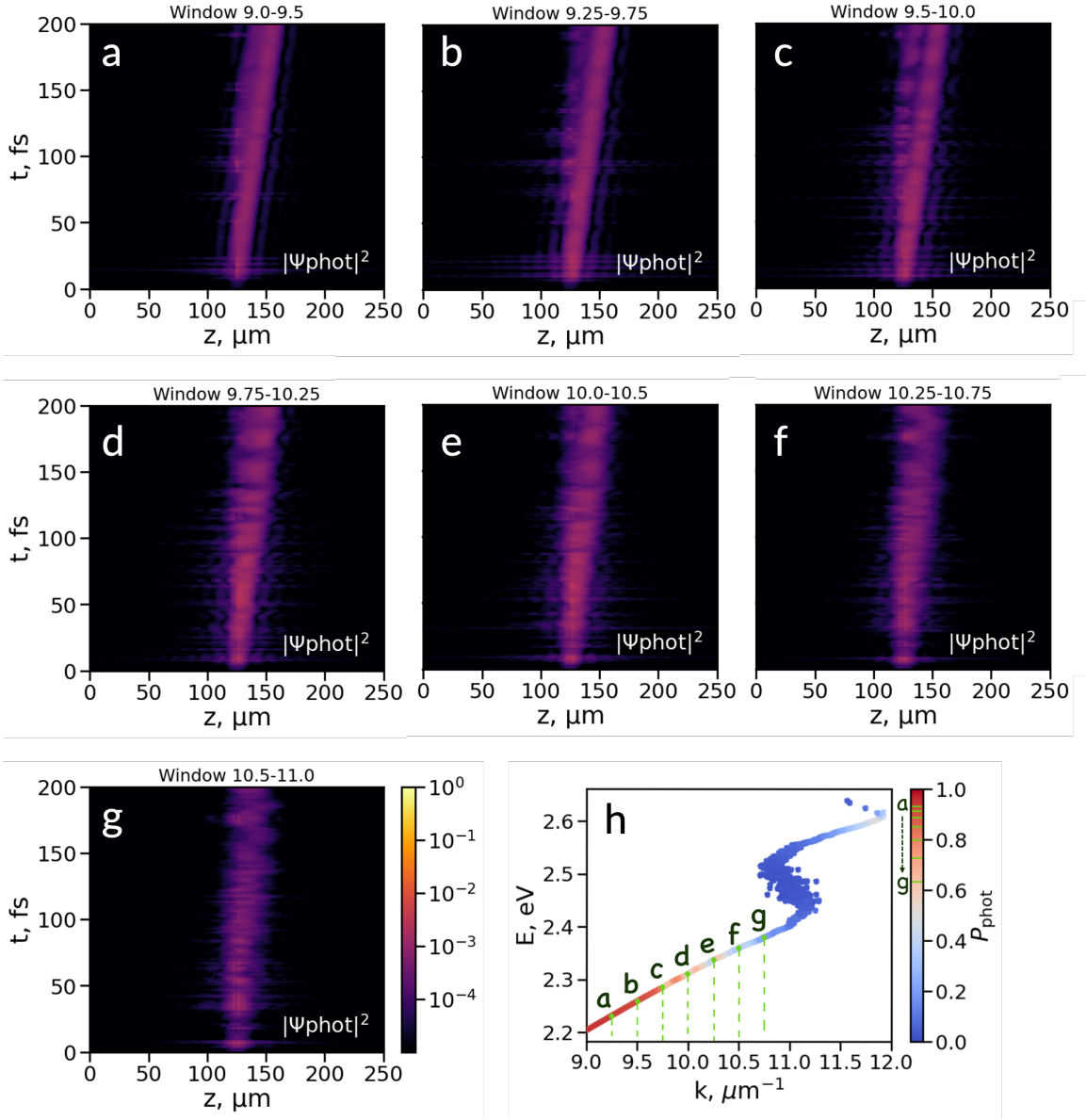
Figure 14. Panels **a-g**: Time-space maps of the probability amplitude of the partial photonic wave function $|\Psi_{\text{phot}}^{\text{part}}(z,t)|^2$ extracted through different wave vector windows in molecular dynamics simulations of $N = 1024$ molecules. Panel **h**: The position of the centre point of each window corresponding to the position on the dispersion curve.

To analyze the transport regime of polaritons along the LP branch, we computed the mean squared displacements (MSD_w) of the partial *photonic* wave function $|\Psi_{\text{phot}}^{\text{part}}|^2$ extracted from different wave vector windows (Figure 15**a-g**). For each wave vector range, MSD_w was obtained in both the MD simulations (black dashed lines) and simulations of static two-level systems (cyan lines), allowing a direct comparison of the two approaches.
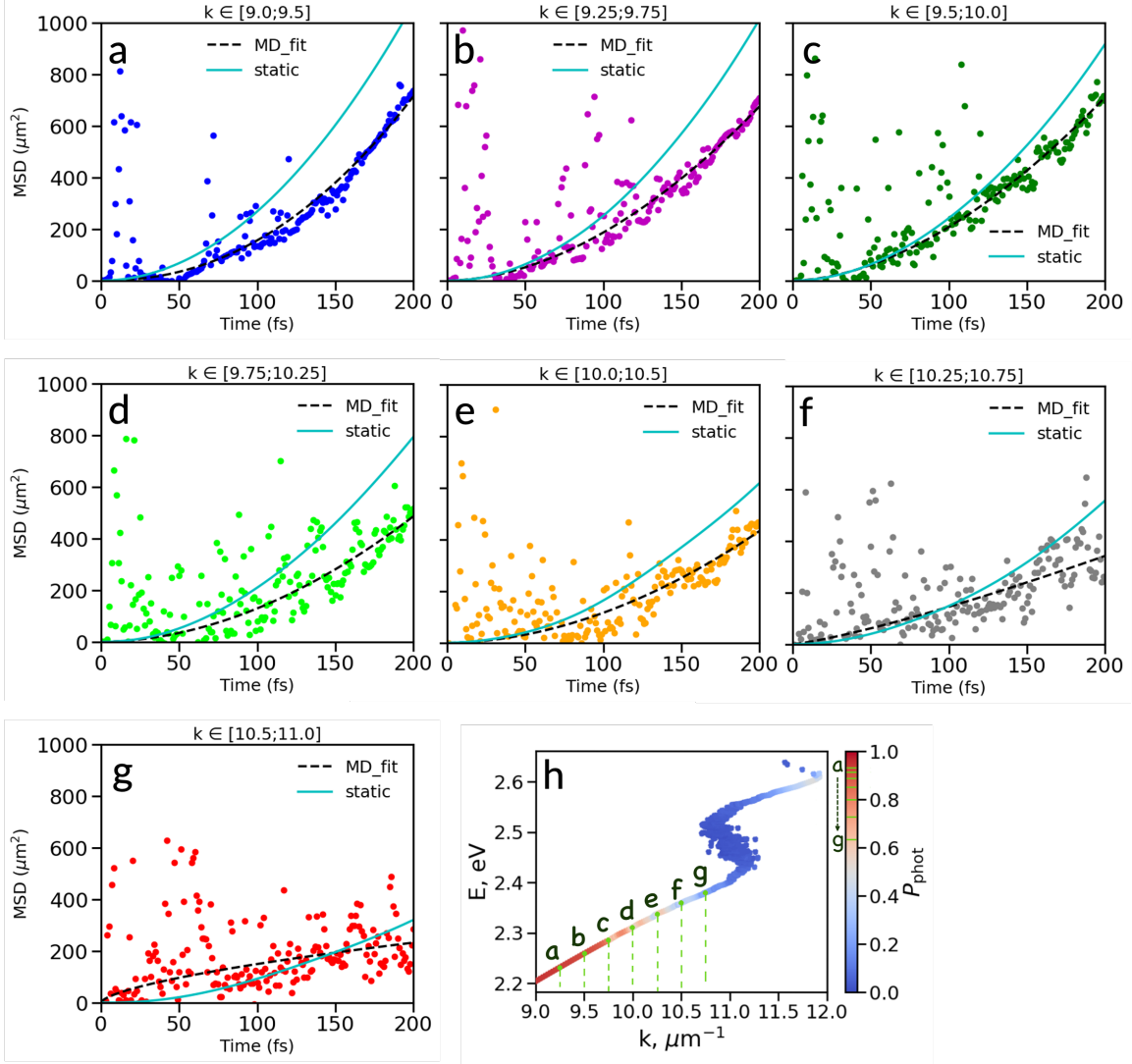
Figure 15. Panels **a-g**: Mean squared displacement, $\text{MSD}_w(t) - \text{MSD}_w(0)$, of partial photonic wave function $|\Psi_{\text{phot}}^{\text{part}}(z,t)|^2$ extracted through different wave vector windows in molecular dynamics simulations of $N = 1024$ molecules. Dashed lines are fits of the dots to $D_\beta \cdot t^\beta$ (Equation 8). The cyan lines correspond to static simulations of two-level systems with excitation energy disorder. Panel **h**: The position of the centre point of each window corresponding to the position on the dispersion figure.

As discussed in Section 4.3.1, in the static two-level simulations, the MSD_w shows a smooth, parabolic increase across all wave vector windows, indicating a purely ballistic transport regime (Figure 13). In contrast, in the MD simulations, significant deviations emerge as time progresses, particularly at the windows with larger k_z values (e.g., Figures 15f and 15g). The MSD_w growth in these regions becomes slower and less uniform compared to the static case, reflecting the influence of dynamical effects such as molecular vibrations and thermal fluctuations. These changes demonstrate that the ballistic transport observed in the static two-level simulations is altered in the MD framework, which incorporates a more realistic description of the environment. The differences between the two approaches underscore the im-

portance of including dynamics of molecules and a realistic description of molecules, in particular vibrations, to capture the complexity of polariton transport.

To further analyze the transport behavior observed in the MSD results, we fitted the MSD in Figures 15 to the Equation 8 and extracted the transport exponents β as a function of the photonic mode contribution $|\alpha_{\mathrm{ph}}|^2$. Figure 16 provides a direct comparison between the experimental results (Figure 16a) and the MD simulations (Figure 16b). In both cases, the transition from ballistic ($\beta \approx 2$) to diffusive transport ($\beta \approx 1$) becomes evident as $|\alpha_{\mathrm{ph}}|^2$ decreases, which correspond to the wave vector regions with reduced photonic weight, unlike static simulations, for which the transport exponent remains close to two within the whole range of LP states with well-defined wave vectors (Figure 13d).
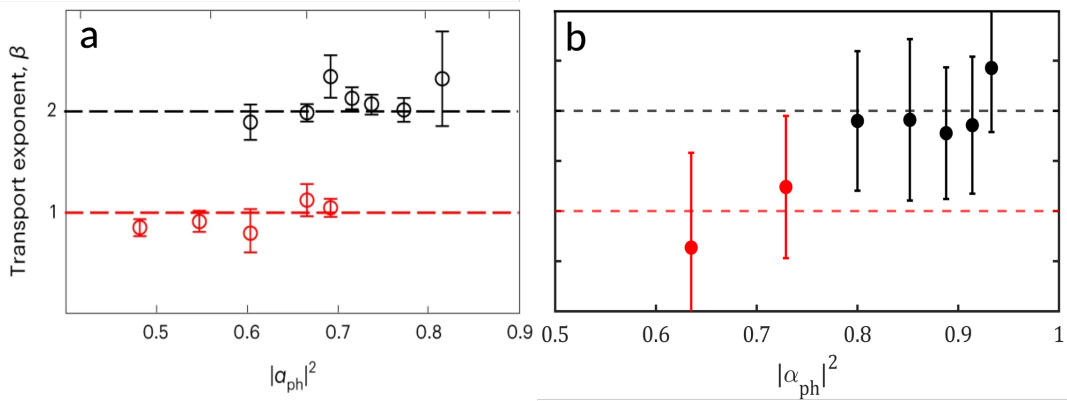

Figure 16. Panel **a** and **b**: The transport exponent as a function of the cavity modes contribution $|\alpha_{\mathrm{ph}}|^2$ to polaritonic states, extracted from the experiment (**a**) and MD simulations (**b**). Panel **a** is reproduced with permission from Balasubrahmaniyam *et al.*, *Nat. Mater.*, **22**, 338-344 (2023). Copyright 2023 Springer Nature Ltd. The error bars in panel **b** are standard deviations of five runs.

To fully understand the shift from ballistic to diffusive transport, it is crucial to examine the underlying mechanisms at play. Molecular vibrations are key here, as they enable non-adiabatic couplings that facilitate transitions, specifically, population exchange between the LP states and the dark states. The strength of these couplings is highly sensitive to the energy difference between the states involved.[71] LP states with a stronger excitonic character (i.e., those closer in energy to the dark states) experience more frequent exchanges of energy. This, in turn, amplifies the transfer of population towards the dark states. Because these dark states lack group velocity, they effectively impede transport efficiency.[34]

The impact of this vibration-driven population redistribution is clearly evident when comparing the MD simulations with static model simulations. The results from static simulation only show ballistic transport regime across the LP branch. However, once molecular vibrations are incorporated into the MD simulations, we

observe a transition from ballistic towards diffusive transport as $|\alpha_{\mathrm{ph}}|^2$ decreases. The agreement between experimental results[16] (Figure 16a) and simulations (Figure 16b) confirms that the transition is strongly correlated with the diminishing contribution of cavity modes ($|\alpha_m|^2$) to the polaritonic states.

The inclusion of molecular vibrations in MD simulations offers a significantly more nuanced and complete picture of polariton transport, highlighting the complex interplay between light-matter interactions and the surrounding dynamic environment in determining energy transport characteristics. Our findings show that static excitation energy disorder alone, a previously suggested explanation, is insufficient to account for the observed transition from ballistic to diffusive transport. Consequently, our findings emphasize the critical importance of considering both vibrational and molecular dynamics for a comprehensive understanding and eventual optimization of polariton transport.

5   Conclusions

In this thesis, excitation energy transport in a system of organic molecules coupled to Bloch Surface Waves in a one-dimensional photonic crystal was investigated, with a particular focus on how the transport undergoes a transition between ballistic to diffusive regimes. We employed a multi-scale computational approach, integrating MD simulations with a QM/MM framework, to dissect the influence of dynamics of molecules on polariton transport under these strong coupling conditions.

Initially, we used a simplified static two-level systems model to benchmark our approach, verifying the calculated polariton dispersion against experimental data. This initial model successfully reproduced the characteristic LP and UP branches, confirming its ability to capture the fundamental energetic landscape of the system. However, analysis of the MSD revealed a purely ballistic transport regime across all seven ranges of wave vectors, failing to reproduce the experimentally observed transition from ballistic transport to diffusive transport. This discrepancy underscored a key limitation: the static model inherently neglects the dynamic fluctuations present in real molecular systems, such as molecular vibrations and variations in excitation energy, which are crucial for a realistic description of transport.

To overcome this limitation, we incorporated MD simulations, which explicitly account for the effects of dynamic disorder and molecular vibrations. By examining the mean squared displacement of partial photonic wave functions extracted from specific wave vector windows, we observed a clear modification of transport behavior. At low wave vectors, where the polariton behavior is dominated by its photonic component, transport remained ballistic. However, at higher wave vectors, where the excitonic contribution becomes more significant, the MSD deviated from the parabolic trajectory characteristic of ballistic transport. Analysis of the transport exponents (β) derived from the MD simulations shows a gradual shift from ballistic transport ($\beta \approx 2$) towards diffusive behavior ($\beta \approx 1$) at larger k_z values. This result is in good agreement with experimental observations, highlighting the crucial role of dynamic molecular effects in driving the transition between transport regimes. In particular, specific vibrational modes of the organic molecules are responsible for the population transfers between polariton states and dark states via non-adiabatic coupling.

In conclusion, our work demonstrates that static excitation energy disorder alone is insufficient to explain the experimentally observed shift in polariton transport. Instead, molecular vibrations and changes in excitation energy, i.e. dynamic factors, cause the transition, as shown by our MD simulations. By moving beyond the

constraints of static models, this study provides a more nuanced and accurate picture of polariton transport in these hybrid light-matter systems, emphasizing the critical role of dynamic effects.

References

1. UN, Take Action for the Sustainable Development Goals. https://www.un.org/sustainabledevelopment/sustainable-development-goals/, Accessed: 2024-05-15.

2. Madsen, D. N.; Hansen, J. P. Outlook of solar energy in Europe based on economic growth characteristics. *Renewable and Sustainable Energy Reviews* **2019**, *114*, 109306.

3. Gervais, E.; Shammugam, S.; Friedrich, L.; Schlegl, T. Raw material needs for the large-scale deployment of photovoltaics–Effects of innovation-driven roadmaps on material constraints until 2050. *Renewable and Sustainable Energy Reviews* **2021**, *137*, 110589.

4. Smith, B. L.; Woodhouse, M.; Horowitz, K. A.; Silverman, T. J.; Zuboy, J.; Margolis, R. M. *Photovoltaic (PV) module technologies: 2020 benchmark costs and technology evolution framework results*; 2021.

5. Fazal, M.; Rubaiee, S. Progress of PV cell technology: Feasibility of building materials, cost, performance, and stability. *Solar Energy* **2023**, *258*, 203–219.

6. NREL, Photovoltaic research - The best research-cell efficiency. https://www.nrel.gov/pv/cell-efficiency.html, Accessed: 2024-04-04.

7. Richter, A.; Hermle, M.; Glunz, S. W. Reassessment of the limiting efficiency for crystalline silicon solar cells. *IEEE journal of photovoltaics* **2013**, *3*, 1184–1191.

8. Sampaio, P. G. V.; González, M. O. A. Photovoltaic solar energy: Conceptual framework. *Renewable and sustainable energy reviews* **2017**, *74*, 590–601.

9. Mikhnenko, O. V.; Blom, P. W.; Nguyen, T.-Q. Exciton diffusion in organic semiconductors. *Energy & Environmental Science* **2015**, *8*, 1867–1888.

10. Agranovich, V.; La Rocca, G. C. Electronic excitations in organic microcavities with strong light–matter coupling. *Solid state communications* **2005**, *135*, 544–553.

11. Clean Energy Reviews Most Efficient Solar Panels. 2024; https://www.cleanenergyreviews.info/blog/most-efficient-solar-panels, Accessed: 2024-12-18.

12. Mihailetchi, V. D.; Xie, H.; de Boer, B.; Koster, L. A.; Blom, P. W. Charge transport and photocurrent generation in poly (3-hexylthiophene): methanofullerene bulk-heterojunction solar cells. *Advanced Functional Materials* **2006**, *16*, 699–708.

13. Jørgensen, M.; Norrman, K.; Krebs, F. C. Stability/degradation of polymer solar cells. *Solar energy materials and solar cells* **2008**, *92*, 686–714.

14. Karl, N. *Organic electronic materials: conjugated polymers and low molecular weight organic solids*; Springer, 2001; pp 283–326.

15. Hopfield, J. Theory of the contribution of excitons to the complex dielectric constant of crystals. *Physical Review* **1958**, *112*, 1555.

16. Balasubrahmaniyam, M.; Simkhovich, A.; Golombek, A.; Sandik, G.; Ankonina, G.; Schwartz, T. From enhanced diffusion to ultrafast ballistic motion of hybrid light–matter excitations. *Nature Materials* **2023**, *22*, 338–344.

17. Kena-Cohen, S.; Forrest, S. R. Giant Davydov splitting of the lower polariton branch in a polycrystalline tetracene microcavity. *Physical Review BâCondensed Matter and Materials Physics* **2008**, *77*, 073205.

18. Rider, M.; Barnes, W. Something from nothing: linking molecules with virtual light. *Contemporary Physics* **2021**, *62*, 217–232.

19. Berghuis, A. M.; Halpin, A.; Le-Van, Q.; Ramezani, M.; Wang, S.; Murai, S.; Gómez Rivas, J. Enhanced delayed fluorescence in tetracene crystals by strong light-matter coupling. *Advanced Functional Materials* **2019**, *29*, 1901317.

20. Agranovich, V.; Gartstein, Y. N. Nature and dynamics of low-energy exciton polaritons in semiconductor microcavities. *Physical Review B* **2007**, *75*, 075302.

21. Sapienza, L.; Vasanelli, A.; Ciuti, C.; Manquest, C.; Sirtori, C.; Colombelli, R.; Gennser, U. Photovoltaic probe of cavity polaritons in a quantum cascade structure. *Applied physics letters* **2007**, *90*.

22. Khitrova, G.; Gibbs, H.; Kira, M.; Koch, S. W.; Scherer, A. Vacuum Rabi splitting in semiconductors. *Nature physics* **2006**, *2*, 81–90.

23. Törmä, P.; Barnes, W. L. Strong coupling between surface plasmon polaritons and emitters: a review. *Reports on Progress in Physics* **2014**, *78*, 013901.

24. Bhuyan, R.; Lednev, M.; Feist, J.; Börjesson, K. The Effect of the Relative Size of the Exciton Reservoir on Polariton Photophysics. *Advanced Optical Materials* **2024**, *12*, 2301383.

25. Luk, H. L.; Feist, J.; Toppari, J. J.; Groenhof, G. Multiscale molecular dynamics simulations of polaritonic chemistry. *Journal of chemical theory and computation* **2017**, *13*, 4324–4335.

26. Ma, C.; Peng, D.; Bai, X.; Liu, S.; Luo, L. A review of optical fiber sensing technology based on thin film and Fabry–Perot cavity. *Coatings* **2023**, *13*, 1277.

27. Pandya, R.; Ashoka, A.; Georgiou, K.; Sung, J.; Jayaprakash, R.; Renken, S.; Gai, L.; Shen, Z.; Rao, A.; Musser, A. J. Tuning the coherent propagation of organic exciton-polaritons through dark state delocalization. *Advanced Science* **2022**, *9*, 2105569.

28. Sinibaldi, A.; Danz, N.; Descrovi, E.; Munzert, P.; Schulz, U.; Sonntag, F.; Dominici, L.; Michelotti, F. Direct comparison of the performance of Bloch surface wave and surface plasmon polariton sensors. *Sensors and Actuators B: Chemical* **2012**, *174*, 292–298.

29. Liscidini, M.; Gerace, D.; Sanvitto, D.; Bajoni, D. Guided Bloch surface wave polaritons. *Applied Physics Letters* **2011**, *98*.

30. Lerario, G.; Cannavale, A.; Ballarini, D.; Dominici, L.; De Giorgi, M.; Liscidini, M.; Gerace, D.; Sanvitto, D.; Gigli, G. Room temperature Bloch surface wave polaritons. *Optics letters* **2014**, *39*, 2068–2071.

31. Schwartz, T.; Hutchison, J. A.; Leonard, J.; Genet, C.; Haacke, S.; Ebbesen, T. W. Polariton Dynamics under Strong Light-Molecule Coupling. *ChemPhysChem* **2013**, *14*, 125–131.

32. Pandya, R. et al. Microcavity-like exciton-polaritons can be the primary photoexcitation in bare organic semiconductors. *Nat. Commun.* **2021**, *12*, 6519.

33. Pandya, R.; Ashoka, A.; Georgiou, K.; Sung, J.; Jayaprakash, R.; Renken, S.; Gai, L.; Shen, Z.; Rao, A.; Musser, A. J. Tuning the Coherent Propagation of Organic Exciton-Polaritons through Dark State Delocalization. *Adv. Sci.* **2022**, *9*, 2105569.

34. Sokolovskii, I.; Tichauer, R. H.; Morozov, D.; Feist, J.; Groenhof, G. Multi-scale molecular dynamics simulations of enhanced energy transfer in organic molecules under strong coupling. *Nature Communications* **2023**, *14*, 6613.

35. Jentschura, U. D.; Adkins, G. S. *Quantum Electrodynamics: Atoms, Lasers and Gravity*; World Scientific, 2022.

36. Allen, M. P.; Tildesley, D. J. *Computer simulation of liquids*; Oxford university press, 2017.

37. Allen, M. P.; others Introduction to molecular dynamics simulation. *Computational soft matter: from synthetic polymers to proteins* **2004**, *23*, 1–28.

38. Frenkel, D.; Smit, B. *Understanding molecular simulation: from algorithms to applications*; Elsevier, 2023; pp 98–106.

39. Wang, X.; Ramírez-Hinestrosa, S.; Dobnikar, J.; Frenkel, D. The Lennard-Jones potential: when (not) to use it. *Physical Chemistry Chemical Physics* **2020**, *22*, 10624–10633.

40. Groenhof, G. Introduction to QM/MM simulations. *Biomolecular simulations: methods and protocols* **2013**, 43–66.

41. Bio Excel Center of Excellence Virtual Workshop: Best Practices in QM/MM Simulation of Biomolecular Systems. 2024; Accessed: 2024-05-21.

42. Groenhof, G.; Modi, V.; Morozov, D. Observe while it happens: catching photoactive proteins in the act with non-adiabatic molecular dynamics simulations. *Current Opinion in Structural Biology* **2020**, *61*, 106–112.

43. Jaynes, E. T.; Cummings, F. W. Comparison of quantum and semiclassical radiation theories with application to the beam maser. *Proc. IEEE* **1963**, *51*, 89–109.

44. Tavis, M.; Cummings, F. W. Approximate solutions for an N-molecule radiation-field Hamiltonian. *Phys. Rev.* **1969**, *188*, 692–695.

45. Galego, J.; Garcia-Vidal, F. J.; Feist, J. Cavity-Induced Modifications of Molecular Structure in the Strong-Coupling Regime. *Phys. Rev. X* **2015**, *5*, 041022.

46. Luk, H. L.; Feist, J.; Toppari, J. J.; Groenhof, G. Multiscale Molecular Dynamics Simulations of Polaritonic Chemistry. *J. Chem. Theory Comput.* **2017**, *13*, 4324–4335.

47. Sakoda, K. *Optical Properties of Photonic Crystals*; Optical Sciences; Springer Berlin Heidelberg, 2005.

48. Michetti, P.; Rocca, G. C. L. Polariton states in disordered organic microcavities. *Phys. Rev. B.* **2005**, *71*, 115320.

49. Ehrenfest, P. Bemerkung über die angenäherte Gültigkeit der klassischen Mechanik innerhalb der Quantenmechanik. *Z. Phys.* **1927**, *45*, 445–457.

50. Sokolovskii, I.; Goenhof, G. Non-Hermitian molecular dynamics simulations of exciton-polaritons in lossy cavities. *J. Chem. Phys.* **2024**, *160*, 092501.

51. Granucci, G.; Persico, M.; Toniolo, A. Direct semiclassical simulation of photochemical processes with semiempirical wave functions. *J. Chem. Phys.* **2001**, *114*, 10608–10615.

52. Somaschi, N.; Mouchliadis, L.; Coles, D.; Perakis, I. E.; Lidzey, D. G.; Lagoudakis, P. G.; Savvidis, P. G. Ultrafast polariton population build-up mediated by molecular phonons in organic microcavities. *Appl. Phys. Lett.* **2011**, *99*, 143303.

53. National Center for Biotechnology Information PubChem Compound Summary for CID 6099, Methylene Blue. https://pubchem.ncbi.nlm.nih.gov/compound/Methylene-Blue, 2024; Accessed: 2024-11-21.

54. Hohenberg, P.; Kohn, W. Imhomogeneous Electron Gas. *Phys. Rev.* **1964**, *136*, 864–871.

55. Runge, E.; Gross, E. K. U. Density-Functional Theory for Time-Dependent Systems. *Phys. Rev. Lett.* **1984**, *52*, 997–1000.

56. Becke, A. D. Density-functional thermochemistry. V. Systematic optimization of exchange-correlation functionals. *J. Chem. Phys.* **1997**, *107*, 8554–8560.

57. Dunning, T. H. Basis Functions for Use in Molecular Calculations. I. Contractions of (9s5p) Atomic Basis Sets for the First-Row Atoms. *J. Chem. Phys.* **1970**, *53*, 2823–2833.

58. Jorgensen, W. L.; Chandrasekhar, J.; Madura, J. D.; Impey, R. W.; Klein, M. L. Comparison of simple potential functions for simulatin liquid water. *J. Chem. Phys.* **1983**, *79*, 926–935.

59. Bayly, C. I.; Cieplak, P.; Cornell, W. D.; Kollman, P. A. A well-behaved electrostatic potential bsed method using charge restraints for deriving atomic charges - the RESP model. *J. Phys. Chem.* **1993**, *97*, 10269–10280.

60. Tomasi, J.; Mennucci, B.; Cammi, R. Quantum Mechanical Continuum Solvation Models. *Chem. Rev.* **2005**, *105*, 2999–3094.

61. Essmann, U.; Perera, L.; Berkowitz, M. L.; Darden, T.; Lee, H.; Pedersen, L. G. A smooth particle mesh Ewald potential. *J. Chem. Phys* **1995**, *103*, 8577–8592.

62. Bussi, G.; Donadio, D.; Parrinello, M. Canonical sampling through velocity rescaling. *J. Chem. Phys.* **2007**, *126*, 014101.

63. Berendsen, H.; Postma, J.; van Gunsteren, W.; la, A. D.; Haak, J. Molecular dynamics with coupling to an external bath. *J. Chem. Phys.* **1984**, *81*, 3684–3690.

64. Whang, T.-J.; Huang, H.-Y.; Hsieh, M.-T.; Chen, J.-J. Laser-induced silver nanoparticles on titanium oxide for photocatalytic degradation of methylene blue. *International journal of molecular sciences* **2009**, *10*, 4707–4718.

65. Hou, S.; Khatoniar, M.; Ding, K.; Qu, Y.; Napolov, A.; Menon, V. M.; Forrest, S. R. Ultralong-range energy transport in a disordered organic semiconductor at room temperature via coherent exciton-polariton propagation. *Advanced Materials* **2020**, *32*, 2002127.

66. Agranovich, V. M.; Litinskaia, M.; Lidzey, D. G. Cavity polaritons in microcavities containing disordered organic semiconductors. *Physical Review B* **2003**, *67*, 085311.

67. Agranovich, V. M.; Litinskaia, M.; Lidzey, D. G. Cavity polaritons in microcavities containing disordered organic semiconductors. *Phys. Rev. B* **2003**, *67*, 085311.

68. Litinskaya, M.; Reineker, P.; Agranovich, V. M. Fast polariton relaxation in strongly coupled organic microcavities. *J. Lumin.* **2004**, *110*, 364–372.

69. Berghuis, A. M.; Tichauer, R. H.; de Jong, L. M.; Sokolovskii, I.; Bai, P.; Ramezani, M.; Murai, S.; Groenhof, G.; GoÌmez Rivas, J. Controlling exciton propagation in organic crystals through strong coupling to plasmonic nanoparticle arrays. *ACS photonics* **2022**, *9*, 2263–2272.

70. Xu, D.; Mandal, A.; Baxter, J. M.; Cheng, S.-W.; Lee, I.; Su, H.; Liu, S.; Reichman, D. R.; Delor, M. Ultrafast imaging of polariton propagation and interactions. *Nature Communications* **2023**, *14*, 3881.

71. Tichauer, R. H.; Morozov, D.; Sokolovskii, I.; Toppari, J. J.; Groenhof, G. Identifying vibrations that control non-adiabatic relaxation of polaritons in strongly coupled molecule–cavity systems. *The Journal of Physical Chemistry Letters* **2022**, *13*, 6259–6267.